Molecular glue degrader function of SPOP enhances STING-dependent immunotherapy efficacy in melanoma models

Zhichuan Zhu,^{1,2†} Xin Zhou,^{1,3†} Max Xu,^{1,3} Jianfeng Chen,^{1,2} Kevin C. Robertson,^{1,4} Gatphan Atassi,¹ Mark G. Woodcock,^{1,5} Allie C. Mills,⁶ Laura E. Herring,⁶ Gianpietro Dotti,^{1,3*} and Pengda Liu^{1,2*}

† These authors contribute equally

Gianpietro Dotti, MD 5202 Marsico Hall 125 Mason Farm Road, CB# 7599 The University of North Carolina at Chapel Hill

Chapel Hill, NC 27599 Phone: 919-962-8279

Email: gianpi@email.unc.edu

Pengda Liu, PhD

21-246 Lineberger Building 450 West Drive, CB#7295

The University of North Carolina at Chapel

Hill

Chapel Hill, NC 27599 Phone: 919-966-3522

Email: pengda liu@med.unc.edu

Competing interests: Dr. Dotti serves in the SAB of Ouspacebio and NanoCell. No potential conflicts of interest were disclosed by the other authors.

Key words: SPOP, STING, 6lc, molecular glue, immune therapy, melanoma

¹Lineberger Comprehensive Cancer Center, The University of North Carolina at Chapel Hill, Chapel Hill, NC 27599, USA

²Department of Biochemistry and Biophysics, The University of North Carolina at Chapel Hill, Chapel Hill, NC 27599, USA

³Department of Microbiology and Immunology, The University of North Carolina at Chapel Hill, Chapel Hill, NC 27599, USA

⁴Department of Pharmacology, The University of North Carolina at Chapel Hill, Chapel Hill, NC 27599, USA

⁵Division of Oncology, Department of Medicine, The University of North Carolina at Chapel Hill, Chapel Hill, NC 27599, USA.

⁶UNC Proteomics Core Facility, Department of Pharmacology, The University of North Carolina at Chapel Hill, Chapel Hill, NC 27599, USA

^{*}Corresponding author.

Abstract

The E3 ligase SPOP plays a context-dependent role in cancer by targeting specific cellular proteins for degradation, thereby influencing cell behavior. However, its role in tumor immunity remains largely unexplored. In this study, we revealed that SPOP targeted the innate immune sensor STING for degradation in a CK1γ phosphorylation-dependent manner to promote melanoma growth. Stabilization of STING by escaping SPOP-mediated degradation enhanced anti-tumor immunity by increasing IFN production and ISG expression. Notably, small-molecule SPOP inhibitors not only blocked STING recognition by SPOP, but also acted as molecular glues, redirecting SPOP to target neo-substrates such as CBX4 for degradation. This CBX4 degradation led to increased DNA damage, which in turn activated STING and amplified innate immune responses. In a xenografted melanoma B16 tumor model, single-cell RNA-seq analysis demonstrated that SPOP inhibition induced the infiltration of immune cells associated with anti-PD1 responses. Consequently, SPOP inhibitors synergized with immune checkpoint blockade to suppress B16 tumor growth in syngeneic murine models and enhanced the efficacy of CD19-CAR-T therapy. Our findings highlight a molecular glue degrader property of SPOP inhibitors, with potential implications for other E3 ligase-targeting small molecules designed to disrupt protein-protein interactions.

Introduction

The ubiquitin–proteasome pathway is a major mechanism for regulated protein turnover. Among E1, E2, and E3 enzymes (1), E3 ubiquitin ligases confer substrate specificity by recruiting target proteins for ubiquitination and subsequent degradation. SPOP (speckle-type POZ protein), together with Rbx1 and Cullin 3, forms a Cullin-Ring E3 ligase complex, with SPOP serving as the substrate recognition subunit. SPOP targets diverse proteins for ubiquitination and degradation, including transcription modulators (SRC3 (2), DEK (3), ATF2 (4), ERG (5, 6), EWS::FLI1 (7) and BRD4 (8, 9)), enzymes (TRIM24 (3) and PTEN (10)), hormone receptors (AR (11)), apoptotic regulators (Daxx (10)), and cell cycle proteins (Cdc20 (12), cyclin E (13)). Beyond degradation, SPOP mediates non-degradative ubiquitination, such as HIPK2 activation (14), K63-linked 53BP1 ubiquitination to impair DNA repair (15), and LMNB2 priming for WDR26-mediated degradation (16). Additionally, SPOP can function independently of its E3 ligase activity, for example by binding and stabilizing ACE2 to facilitate SARS-CoV-2 infection (17).

The pathological role of SPOP in cancer is context-dependent. In prostate cancer, SPOP mutations occur in ~10% of patients, where it acts as a tumor suppressor by degrading oncogenic transcription factors, including ERG (5, 6), DEK (3), and TRIM24 (3), and by mediating PARP inhibitor-induced tumor suppression via STING stabilization (18). In Ewing sarcoma, SPOP similarly suppresses tumors by targeting the EWS::FLI1 onco-fusion protein (7). In contrast, SPOP exhibits oncogenic activity in kidney cancer by negatively regulating PTEN (10) and LATS1 (19). While SPOP's regulation of intrinsic cellular programs is well documented, its role in immunity and the tumor microenvironment is less clear. SPOP has been reported to inhibit Toll-like receptor signaling (20) by modulating MyD88 ubiquitination (21) or degradation (22), yet it can also promote an immune-permissive environment by degrading IRF1 (23) or PD-L1 (24), enhancing

immune checkpoint blockade (ICB) efficacy and chemosensitivity (25). Whether and how SPOP controls innate immunity and subsequent immune cell infiltrates in solid tumors remains elusive.

Here, we demonstrate that SPOP acts as an oncogene in melanoma by targeting the innate immune sensor STING for ubiquitination and degradation. Loss of SPOP suppresses B16 tumor growth in a manner dependent on host immunity and tumor-intrinsic STING. Small-molecule SPOP inhibitors 6b and 6lc function as molecular glue degraders, recruiting CBX4 to mediate SPOP degradation, which induces DNA damage and activates STING. In B16 xenografts, scRNA-seq revealed that SPOP inhibitor–mediated STING stabilization enhances immune cell infiltration and potentiates anti-PD1 responses, improving the efficacy of both ICB and CAR-T therapies. Together, these findings identify a molecular glue mechanism for SPOP inhibitors and support their potential to sensitize tumors to immunotherapy.

Results

An intact immune microenvironment is crucial for suppressing B16 tumor growth following SPOP depletion

While SPOP's roles in prostate and kidney cancers are well established, its function in melanoma remains unclear. Similar to human RCC (renal cell carcinomas) 786-O and A498 cells, depletion of endogenous SPOP reduced colony formation in human melanoma A2058 and HMCB cells (Supplemental Figure 1, A and B). Likewise, SPOP knockdown in mouse RCC Renca and melanoma B16 cells impaired in vitro growth (Supplemental Figure 1, C-H). In RCC, SPOP exerts oncogenic activity by targeting the tumor suppressor PTEN (10), and TCGA analyses revealed similar patterns of SPOP and PTEN alterations in KIRC and SKCM (Supplemental Figure 11). These results suggest that SPOP may function as an oncogene in melanoma, analogous to its role in RCC.

To assess SPOP's role in tumor immunity, control or SPOP-depleted B16 cells were xenografted into immune-deficient nude mice or immune-competent C57BL/6 mice (Figure 1A). Consistent with in vitro data (Supplemental Figure 1E), SPOP depletion slightly reduced tumor growth in nude mice but markedly suppressed tumor growth in C57BL/6 mice (Figure 1, B-D), suggesting that host T cell immunity is required for SPOP depletion-mediated tumor suppression. Re-expression of SPOP largely rescued tumor growth in C57BL/6 mice, ruling out shRNA off-target effects (Figure 1, E-H). Cytokine profiling of SPOP-depleted human melanoma A2058 cells revealed increased expression of interferon-stimulated genes (ISGs), including IFIT1, CXCL10, and MX1, validated by RT-PCR (Figure 2, A-C). This was supported by xenografted SPOP-depleted B16 tumors, where SPOP loss led to increased CCL5 and CXCL10 expression (Supplemental Figure 1J). mRNA profiling of SPOP-depleted B16 cells also revealed upregulated

ISGs (Supplemental Figure 1K). Given that type I interferons and ISGs mediate tumor innate immune activation and recruit immune infiltrates (26, 27), these findings indicate that SPOP depletion enhances tumor innate immunity to suppress melanoma growth. In this study, we focus on melanoma and RCC to determine whether SPOP regulates tumor immunity.

SPOP-depletion enhances cellular responses to DNA stimulation

Since cytosolic DNA-sensing pathways drive ISG expression (28), we tested whether SPOP depletion alters responses to DNA stimulation. DNA-sensing is a ubiquitous innate immune pathway in both immune and tumor cells, initiated when cGAS detects cytosolic DNA and produces 2'3'-cGAMP, which activates STING to trigger TBK1/IRF3-dependent IFNβ and ISG expression (29-32). SPOP depletion markedly enhanced ISD90-induced STING activation, as shown by increased pSTING, an effect reversed by SPOP re-expression in HMCB melanoma cells (Figure 2D). Similar results were observed in RCC 786-O cells, where SPOP loss augmented STING signaling, increased IFNβ transcription, and upregulated multiple ISGs, including CCL5, CXCL10, OAS1, IFIT1, and IFI44 (Supplemental Figure 1, L-R). SPOP depletion also potentiated 2'3'-cGAMP- and diABZi (33)-induced STING activation and ISG production (Supplemental Figure 1, S-Z). Importantly, re-introducing SPOP largely reversed these effects (Supplemental Figure 1, Z1 and Z2). Collectively, these findings indicate that SPOP depletion sensitizes cells to cytosolic DNA stimulation by enhancing cGAS/STING signaling.

SPOP earmarks STING for ubiquitination and degradation

The cytosolic DNA-sensing pathway primarily involves cGAS, STING, TBK1, and IRF3 (32). To determine how SPOP depletion enhances DNA sensing, we silenced endogenous SPOP using

multiple independent shRNAs/sgRNAs. SPOP loss consistently increased STING protein levels, but not those of cGAS, TBK1, or IRF3, across human melanoma (A2058, HMCB, MeWo), mouse melanoma (B16), human RCC (A498, 786-O, UMRC6), mouse RCC (Renca), and HEK293 cells (Figure 3, A-C and F, Supplemental Figure 2, A-H). Other DNA sensors, including DDX41 and IFI16, were minimally affected. SPOP depletion did not alter STING mRNA levels (Supplemental Figure 2I), suggesting post-transcriptional regulation. Re-expression of shSPOP/sgSPOP-resistant SPOP restored STING to baseline, confirming specificity (Figure 3, D, E, G, Supplemental Figure 2, J-L). Conversely, ectopic SPOP expression reduced endogenous and exogenous STING, reversible by proteasome inhibition (Figure 3, H-I). Cycloheximide chase assays further demonstrated that SPOP depletion stabilized STING, extending its half-life, which was reversed by SPOP re-expression (Figure 3, J-K, Supplemental Figure 2, N-Q).

SPOP recognizes a degron motif Φ - Π -S-S/T-S/T (Φ , nonpolar; Π , polar) (6, 8). Sequence analysis identified a potential degron "PSTST" in human STING (Figure 3L). Mutation of these residues (S353A/T354A/S355A/T356A; 4A-STING) impaired SPOP binding (Figure 3M). Similarly, in mouse STING, mutation of "PSVLS" serines (S354A/S357A; 2A-mSTING) reduced interaction (Figure 3N). Moreover, SPOP efficiently ubiquitinated WT-STING but not 4A-STING (Figure 3O). Together, these results demonstrate that SPOP directly recognizes the "PSTST" degron to ubiquitinate and degrade STING.

CK1\gamma generates a phospho-degron in STING for SPOP recognition

Multiple S/T residues in the canonical SPOP "Φ-Π-S-S/T-S/T" degron can be phosphorylated to enhance SPOP binding (6-8, 17). Testing CK1 and CK2 isoforms revealed that CK1γ, specifically CK1γ1, promotes STING recognition by SPOP (Figure 4, A and B). CK1γ1 depletion in RCC cells

(A498, 786-o, Caki-1, RCC10) led to STING protein accumulation without affecting STING mRNA (Figure 4, C-E), indicating regulation at the protein level. CK1γ1-induced STING degradation was partially blocked by the proteasome inhibitor MG132 or the cullin neddylation inhibitor MLN4924, but not by the lysosomal inhibitor Baf-A1 (Figure 4F), and required the intact STING degron, as 4A-STING was resistant (Figure 4G). Pharmacological CK1 inhibition (D4476 or Epiblastin A) similarly stabilized STING by reducing CK1γ1-mediated phosphorylation and SPOP binding (Figure 4, H and I, Supplemental Figure 2R). These results indicate CK1γ1 phosphorylates the STING "PSTST" motif to prime it for SPOP-mediated ubiquitination and degradation (Figure 4J).

Evading SPOP-mediated degradation enhances STING activation in innate immunity

We next asked whether STING stabilization by evading SPOP-mediated degradation enhances innate immune activation. Re-expression of WT- or 4A-STING in STING-depleted 786-o cells showed comparable ISD90-induced STING activation (Figure 5A), but RT-PCR revealed that 4A-STING induced significantly lower IFNβ and ISG (CCL5, CXCL10) expression than WT-STING after ISD90 or diABZI stimulation (Figure 5, B and C, Supplemental Figure 3, A-D). This suggested that loss of phosphorylation within the degron impairs STING activation. Consistent with prior reports that TAK1 phosphorylates STING at S355 to facilitate ER-to-ERGIC trafficking (34), S355F-STING failed to rescue STING activation in depleted cells (Supplemental Figure 3E).

To identify mutations that evade SPOP without disrupting activation, we found a T356M-STING mutation in a gastric cancer patient (COSMIC) that disrupted SPOP binding (Figure 5, D and E) and reduced SPOP-mediated ubiquitination (Figure 5F), extending STING half-life (Figure 5, G-I). T356M-STING enhanced ISD90- or diABZI-induced STING activation (Figure 6, A-C,

Supplemental Figure 3F). Similarly, CK1γ1 depletion or pharmacological inhibition (D4476) stabilized STING, boosting diABZI-induced activation and downstream IFNβ and ISG expression (CCL5, CXCL10, OAS1, IFIT1, IFI44) (Figure 6, D-G, Supplemental Figure 3, G-M). These results indicate that evasion of SPOP recognition stabilizes STING, enhancing its activation (Figure 6H).

Pharmacological SPOP inhibition disrupts STING binding to SPOP and enhances STING activation

Since E3 ubiquitin ligases do not exert catalytic activities but only serve to bridge E2 enzymes to specific substrates (35), a few E3 ligase inhibitors have been developed to block a certain E3 ligase binding to its substrates, including Apcin (36) (blocks Cdc20/substrate interactions), Skpin (37) (blocks Skp2/p27 interactions (38)), Nutlin (39) (blocks Mdm2/p53 binding), and DCAF1 inhibitors (40). Interestingly, a small molecule SPOP inhibitor SPOP-IN-6b (6b) was developed for treating kidney cancer where SPOP exerts an oncogenic function (41) and it was further upgraded to SPOP-i-6lc (6lc) (42) through medicinal chemistry optimization. Consistent with the previous study (41), we observed 6b disrupted SPOP interactions with PTEN (Supplemental Figure 4A). We found that 6b similarly disrupted STING binding to SPOP (Supplemental Figure 4B), and 6lc was also able to do so (Figure 7A), further supporting STING as a SPOP substrate.

Disrupting SPOP recognition, treatment with 6b (Figure 7, B and C) or 6lc (Supplemental Figure 4, C and D) stabilized STING in cells. This effect was SPOP-dependent (Supplemental Figure 4, E and F), ruling out off-target effects. STING stabilization was dose-dependent, but at higher 6b/6lc doses, STING levels slightly decreased while activation markers pTBK1 and pIRF3 increased (Figure 7, B and C, Supplemental Figure 4, C and D), consistent with lysosomal

degradation of activated STING (43). Cytokine profiling in 6lc-treated A2058 and B16 cells (Figure 7, D and E) showed a broader and stronger ISG induction compared with SPOP genetic depletion (Figure 2B), indicating pharmacological inhibition more effectively activates STING.

Pharmacological SPOP inhibition induces DNA damage to trigger STING activation

Canonical STING activators include viral/bacterial DNA, apoptotic cells, and damaged genomic or mitochondrial DNA (32). Treatment with 6b significantly increased genomic DNA damage, as shown by comet assays (44) (Figure 7, F and G) and γH2AX foci (Figure 7, H and I); 6lc had similar effects (Figure 7, J and K, Supplemental Figure 4, G and H). DNA damage led to cytosolic dsDNA accumulation (Figure 8A, Supplemental Figure 4I), activating STING and inducing ISGs (Figure 8B, Supplemental Figure 4J). Although 6lc also caused mitochondrial DNA leakage (Supplemental Figure 4K), EtBr-mediated depletion of mitochondrial DNA (45) did not affect STING activation (Supplemental Figure 4, L and M), indicating genomic DNA as the primary activator. Cytosolic dsRNA was unaffected (Supplemental Figure 4, N and O). Knockdown of cGAS or STING abolished 6lc-induced STING activation and ISG induction (Figure 8C, Supplemental Figure 4, P and R). Notably, SPOP genetic depletion did not increase DNA damage (Figure 8, D and E), suggesting that pharmacological inhibition, which preserves SPOP scaffolding while blocking E3 ligase activity (Figure 8F), uniquely induces DNA damage to activate cGAS/STING.

SPOP inhibitors "glue" neo-substrates for SPOP-mediated ubiquitination and degradation to accumulate DNA damage

The distinct DNA damage-inducing effect of SPOP inhibitors versus genetic depletion suggested that 6b/6lc not only block SPOP's interaction with STING but also recruit neo-substrates for degradation (Figure 9A), similar to how lenalidomide acts as a molecular glue for CRBN (46-48). In addition, different lenalidomide derivatives recruit distinct neo-substrates for CRBN binding and degradation (49), supporting the role of E3 ligase inhibitors in controlling E3 substrate specificity. We similarly hypothesize that without 6b or 6lc, SPOP targets STING for ubiquitination and degradation, while 6b/6lc binding to SPOP may on one hand blocks STING binding to SPOP to stabilize STING, and on the other hand recruit neo-substrates to SPOP for degradation, through which 6b/6lc accumulates DNA damage to activate STING. Consistently, 6b/6lc treatment increased ubiquitinated proteins (Supplemental Figure 5A). To identify neosubstrates, we performed quantitative mass spectrometry with K-\varepsilon-GG enrichment comparing 6lctreated and untreated A2058 cells, using SPOP-depleted cells as controls (Figure 9B). Among 3,625 proteins with increased ubiquitination (log2FC ≥1), 182 showed SPOP-dependent increases (Figure 9C), enriched in chromosome organization and DNA damage response pathways (Supplemental Figure 5B). Focusing on DNA damage regulators, 6lc enhanced ubiquitination of CBX4 (chromobox protein homolog 4), ESCO2, GNE, HP1γ, METTL3, and TAOK2 (Figure 9D).

We further hypothesized that SPOP/6lc induced degradation of the true hit(s) should cause DNA damage prior to STING activation. Time-course analysis revealed only CBX4 degradation preceded STING activation in 6lc-treated A2058 and 786-o cells (Figure 10A, Supplemental Figure 5, C and D). 6lc promoted CBX4 K48-linked ubiquitination and proteasomal degradation in a SPOP/Cul3–dependent manner (Figure 10, B and C, Supplemental Figure 5F). CBX4 protein were unaffected by SPOP depletion (Figure 10D), indicating CBX4 is not a natural SPOP substrate; nor by 6lc (Figure 10E), ruling out transcriptional regulation. In vitro pulldown confirmed SPOP

binds CBX4 only in the presence of 6lc (Figure 10F, Supplemental Figure 5, G and H). The CBX4-K114R mutant resisted 6lc-induced ubiquitination and degradation (Supplemental Figure 5, I and J).

CBX4, a SUMO E3 ligase in PRC1 (50), uses its chromodomain and SUMO-interacting domains (SIMs) for function (Figure 10G). Truncation of its C-terminal region abolished 6lc-mediated degradation (Figure 10H), suggesting this region contains the neo-degron. Together, these results support CBX4 as a bona fide neo-substrate for SPOP/6lc, revealing that 6lc functions as a molecular glue recruiting CBX4 to SPOP for degradation, which in turn induces DNA damage.

CBX4 is a neo-substrate for SPOP/6lc to control DNA damage response

We next tested whether SPOP/6lc-induced CBX4 degradation triggers DNA damage. CBX4 depletion increased DNA damage, as shown by elevated pChk1, γH2AX signals, and cytosolic dsDNA/cGAS foci (Figure 11A, Supplemental Figure 6, A-C). Ectopic CBX4 partially rescued 6lc-induced CBX4 degradation, DNA damage, and cytosolic dsDNA accumulation (Figure 11, B-F, Supplemental Figure 6, D-E), reducing STING activation and ISG production (IFNβ, CCL5, CXCL10; Figure 11G). Conversely, CBX4-depleted cells were resistant to 6lc-induced DNA damage and dsDNA accumulation (Supplemental Figure 6, F-H), supporting CBX4 as a key SPOP/6lc neo-substrate mediating STING activation.

CBX4, besides promoting cancer progression (51) and metastasis (52), maintains genome stability via SUMOylation of BMI1 (53), which recruits BMI1 to DNA damage foci (54) for repair (55). Consistently, 6lc reduced CBX4 and BMI1 foci, while ectopic CBX4 restored BMI1 foci and H2AX interactions (Figure 11, H-K). A SUMO E3 ligase-deficient CBX4 mutant (ΔSIM1/2) failed to rescue BMI1 recruitment (Figure 11K, Supplemental Figure 6, I-K). These data support a model

in which 6lc both stabilizes STING by blocking SPOP binding and glues CBX4 to SPOP for degradation, impairing BMI1-mediated DNA repair. The resulting DNA damage activates STING, promoting tumor innate immunity and enhancing immune cell infiltration to improve therapeutic responses (Figure 11L).

SPOP inhibition enhances the anti-tumor effects of checkpoint blockades and CAR-T cells Immune checkpoint blockers (ICB) are pivotal in metastatic melanoma (56, 57), but response rates are influenced by tumor-infiltrating lymphocytes and the tumor microenvironment (58). Since SPOP inhibition stabilizes and activates STING, triggering IFN and ISG production which could promote immune cell infiltration (59), we evaluated whether SPOP inhibitors enhance ICB efficacy in melanoma models. Using the anti-PD1-resistant B16 C57BL/6 model (60, 61), mice were treated daily with the SPOP inhibitor 6b and tumors collected on day 13 for scRNA-seq of FACS-sorted CD45⁺ cells (Figure 12A). 6b treatment increased B cells (cluster 1), plasma cells (cluster 2), macrophages (cluster 3), and memory CD4⁺ T cells (cluster 4), which are associated with anti-PD1 response (Figure 12, B and C, Supplemental Figure 7, A and B) (62-64). CD8⁺ populations were largely unchanged, but PD-L1 expression was upregulated in plasma cells, naïve CD8⁺ T cells, macrophages, and CD36⁺ monocytes (Supplemental Figure 7C).

Functionally, 6b or anti-PD1 alone showed limited efficacy, whereas the combination significantly reduced tumor growth with minimal toxicity (Figure 12, D and E, Supplemental Figure 8A). FACS and IHC analyses confirmed enrichment of intratumoral CD4⁺ T cells, particularly IFNγ⁺ activated cells (Figure 12, F-H, Supplemental Figure 8B), and increased activated CD8⁺ (GrzB⁺) T cells (Figure 12, I and J). Although macrophages increased, 6b shifted polarization from M1 to M2 (Supplemental Figure 8, C-G), suggesting macrophage changes do

not mediate the anti-tumor effect. Similar results were observed using the SPOP inhibitor 6lc (Supplemental Figure 8, H and I).

Importantly, the combination of 6b and anti-PD-1 markedly inhibited WT-B16 tumor growth, but not STING-depleted tumors (Figure 13, A-C), indicating that 6b's anti-tumor effect depends on SPOP/STING signaling. Analysis of the TIGER (Tumor Immunotherapy Gene Expression Resource) further showed that melanoma patients with high SPOP expression had poorer responses to anti-PD-1 therapy (Figure 13D), likely due to reduced STING levels and lower tumor-infiltrating immune cells.

Using the B16-OVA-hCD19 model (61, 65-67), we tested CAR-CD19-T cell therapy with or without 6lc (5 doses, 20 mg/kg) (Figure 14A). The combination of 6lc and CAR-CD19-T cells markedly improved tumor control (Figure 14, B and C) and increased infiltration of both CAR-T and endogenous CD4+ T cells (Figure 14, D-H). These results indicate that SPOP inhibition enhances the efficacy of both ICB and CAR-T therapies by promoting CD4+ T cell-mediated anti-tumor immunity, highlighting its potential to boost diverse immunotherapy approaches.

DISCUSSION

We identified the E3 ligase SPOP as a suppressor of tumor immunity by promoting ubiquitination and degradation of the innate immune sensor STING in melanoma and RCC. Pharmacological SPOP inhibitors 6b and 6lc not only disrupt the SPOP/STING interaction but also act as molecular glues, inducing degradation of neo-substrates. Global K-ε-GG enrichment and LC-MS/MS analyses revealed CBX4 as a neo-substrate of the SPOP/6lc complex. SPOP-dependent CBX4 degradation impairs DNA repair by disrupting CBX4-mediated SUMOylation and BMI1 recruitment, leading to DNA damage and activation of the cGAS/STING pathway, which in turn stimulates innate immune responses. scRNA-seq of 6b-treated B16 xenografts showed increased infiltration of immune cells linked to anti-PD-1 responsiveness. Consistently, SPOP inhibition synergized with anti-PD-1 therapy to suppress tumor growth via enhanced CD4+IFNγ+ T cell infiltration and further boosted CD19-CAR-T efficacy in B16-OVA tumors. These findings establish a molecular glue function for SPOP inhibitors and highlight their promise as immunotherapy adjuvants.

Targeted protein degradation is an emerging therapeutic strategy (68). Unlike PROTACs, which are rationally designed by linking ligands for a protein of interest and an E3 ligase (69), molecular glue degraders are typically discovered serendipitously. Their smaller size confers better delivery, oral bioavailability, and pharmacodynamics. Although ~20 molecular glues have been identified (69), most were found through random screening, as their rational design remains challenging (68). Known molecular glues primarily act through E3 ligases such as DCAF15 (70, 71), DDB1 (72-74) and β-TRCP (75), which promote E3/substrate complex formation. For instance, the β-TRCP glue enhances β-TRCP/β-catenin interaction (75). Whether CRBN-, DCAF15-, or DDB1-associated glues also disrupt native substrate binding remains unclear. Our findings reveal that

SPOP inhibitors 6b and 6lc act through a distinct mechanism-simultaneously blocking endogenous substrate binding while recruiting neo-substrates. As SPOP is a cullin 3 E3 ligase, unlike the cullin 1/4 ligases targeted previously (35), these compounds expand the landscape of molecular glue degraders.

The STING agonist 2'3'-cGAMP has been shown to improve anti-PD1 efficacy in B16 melanoma models (76). Melanoma is generally immune-cold, and predictors of anti-PD1 response include BRCA2 mutations and the IPRES transcriptional signature, rather than mutation burden (77). Combination therapies enhancing CD8⁺ T cell infiltration or PD-L1 expression improve anti-PD1 efficacy (78).

Enhancing CD8⁺ T cell infiltration and tumor PD-L1 expression typically augments anti-PD-1 responses. Here, pharmacological SPOP inhibition stabilizes and activates tumor STING, driving infiltration of active CD4⁺, but not CD8⁺ T cells, thereby improving anti-PD-1 efficacy in B16 melanoma. Although SPOP inhibition increases M2 rather than M1 macrophages, this immunosuppressive shift is counterbalanced by enhanced effector T cell infiltration. While CD4⁺ T cells are traditionally considered helpers for cytotoxic T lymphocyte activation, they can also produce effector cytokines, such as IFNγ, to directly mediate tumor cell killing (79). This mechanism appears to underlie the anti-tumor effects of 6b/6lc observed in our study. Additionally, CD4⁺ T cells can drive humoral immune responses by promoting B cell differentiation and maturation into affinity-matured, class-switched plasma cells (80, 81), consistent with our scRNA-Seq analysis showing increased B and plasma cell populations following 6b treatment. The capacity of CD4⁺ T cells to suppress tumors independently of CD8⁺ T cells through inflammatory cell death has been reported previously (82). Moreover, in a B16-OVA tumor model, SPOP inhibition similarly enhances CD4⁺ CAR-19-T cell tumor infiltration, resulting in improved tumor

control. Collectively, these findings suggest that SPOP inhibition augments CD4⁺ T cell-mediated anti-tumor immunity and support further evaluation of SPOP inhibitors in clinical settings.

MATERIALS AND METHODS

Sex as a biological variable

Only female mice were used in murine melanoma models to ensure data reproducibility. Sex was not considered as a biological variable, as melanoma occurs in both sexes in humans.

Cell culture and transfection

Human RCC cell lines 786-O (from Dr. Qing Zhang, UT Southwestern), A498, Caki-1 (ATCC), RCC10, and UMRC6; mouse RCC line Renca (from Dr. William Kim, UNC); human kidney cell lines HEK293 and HEK293T (ATCC); human melanoma lines A2058, HMCB, and MeWo (from Dr. Deborah DeRyckere, Emory); and mouse melanoma lines B16 and B16-OVA (from Dr. Gianpietro Dotti, UNC) were cultured in DMEM with 10% FBS, 100 U/mL penicillin, and 100 μg/mL streptomycin.

Cells were transfected using Lipofectamine 3000 (L3000150, Thermo Fisher Scientific) or PEI (23966, Polysciences) as described (83, 84). Lentiviral packaging, infection, and selection were performed as previously reported (83, 84), using 200 μg/mL hygromycin (H3274, Sigma-Aldrich) or 2 μg/mL puromycin (BP2956100, Fisher BioReagents). Compounds used include 2'3'-cGAMP (tlrl-nacga23-02, InvivoGen), diABZI (28054, Cayman), D4476 (HY-10324), Epiblastin A (HY-114858), SPOP-IN-6b (HY-122615, MedChemExpress), SPOP-i-6lc (Tocris 7498), Bafilomycin A1 (S1413), and cycloheximide (S6611, Selleck).

Plasmids

Flag-STING constructs (WT, 4A, P352A, S353A, S355F, T356M) and Flag-mSTING (WT, 2A) were generated by overlap PCR and cloned into pcDNA3.0. pBabe-Flag-STING (WT, 4A, S355F)

and pLenti-Flag-STING (WT, T356M) were made by subcloning respective inserts into pBabehygro or pLenti-hygro vectors. HA-CBX4 constructs (WT, ΔSIM1/2, ΔCD, ΔCBox) were generated by overlap PCR from CBX4 cDNA (provided by Dr. Virginia Byers Kraus, Duke University) and cloned into pLenti-GFP-hygro. CMV-GST-CBX4 (WT, K114R) and pET-28a-CBX4 were cloned into CMV-GST and pET-28a vectors, respectively. Flag-, HA-, and GST-SPOP were cloned into pcDNA3-Flag, pcDNA3-HA, and CMV-GST vectors. His-SUMO-avi-SPOP (aa 28–359) was cloned into pExp-His-Sumo-TEV. Flag-cGAS (85), HA-Ub, His-Ub-WT, and K48-Ub (85, 86), Myc-CUL3, CK1/CK2 (7), and Myc-PTEN (87) were described previously. pRSET-6xTR-TUBE was from Addgene (#110313).

Primers

STING-BamHI-F: GACACCGACTCTAGAGGATCCATGCCCCACTCCAGCCTGCA

STING-SalI-Flag-R:

ATCCAGAGGTTGATTGTCGACTCACTTGTCGTCATCGTCTTTGTAGTCAGAGAAATCCGTGCG

GAGAG

mSTING-BgIII-F: GCATAGATCTATGCCATACTCCAACCTGCA

mSTING-SalI-Flag-R:

 ${\tt GCATGTCGACTCACTTGTCGTCATCGTCTTTGTAGTCGATGAGGTCAGTGCGGAGTG}$

STING-4A-F: AGACCTCAGCGGTGCCGCTGCCGCCGCGATGTCCCAAGAGCCTGA

STING-4A-R: TCAGGCTCTTGGGACATCGCGGCGGCAGCGGGCACCGCTGAGGTCT

STING-P352A-F: TGAAGACCTCAGCGGTGGCCAGTACCTCCACGATG

STING-P352A-R: CATCGTGGAGGTACTGGCCACCGCTGAGGTCTTCA

STING-S353A-F: AGACCTCAGCGGTGCCCGCTACCTCCACGATGTCCC

STING-S353A-R: GGGACATCGTGGAGGTAGCGGGCACCGCTGAGGTCT

STING-S355F-F: AGCGGTGCCCAGTACCTTCACGATGTCCCAAGAGC

STING-S355F-R: GCTCTTGGGACATCGTGAAGGTACTGGGCACCGCT

STING-T356M-F: GGTGCCCAGTACCTCCATGATGTCCCAAGAGCCTG

STING-T356M-R: CAGGCTCTTGGGACATCATGGAGGTACTGGGCACC

mSTING-2A-F: CAGTGGCACCTCCTCCCGCCGTACTGGCCCAAGAGCCAAGACTC

mSTING-2A-R: GAGTCTTGGCTCTTGGGCCAGTACGGCGGGAGGAGGTGCCACTG

SPOP-BamHI-F: GCATGGATCCATGTCAAGGGTTCCAAGTCC

SPOP-SalI-R: GCATGTCGACTTAGGATTGCTTCAGGCGTT

BstBI-Avi-tag-SPOP-F:

GCATTTCGAAGGCCTGAATGACATCTTTGAGGCCCAGAAGATCGAGTGGCATGAGAAGGTAG

TGAAATTCTCCTA

XhoI-SPOP-R: GCATCTCGAGTTATGCTGAAGCCAGAGAGC

CBX4-BglII-F: GCATAGATCTGAGCTGCCAGCTGTTGG

CBX4-SalI-R: GCATGTCGACCTACACCGTCACGTACTCC

CBX4-delSIM1-F: AGAACAAGAACGGACGCATGAGCAAATACATGGA

CBX4-delSIM1-R: TCCATGTATTTGCTCATGCGTCCGTTCTTGTTCT

CBX4-delSIM2-F: CCCTCCCGCAGCCCGAGGACTCAGACCTGGATGA

CBX4-delSIM2-R: TCATCCAGGTCTGAGTCCTCGGGCTGCGGGAGGG

CBX4-delCD(1-60)-BglII-F: GCATAGATCTGAACGGCAGGAGCAGCTGAT

CBX4-delCBox(531-560)-SalI-R: GCATGTCGACCAGCGACTCTGCAGGTTCGT

CBX4-delCBox+P3(270-560)-SalI-R:

GCATGTCGACACCGCCTGCATGCCGTTCTCCATGTATTTGCTCATCACGA

CBX4-K114R-F: TTTGGGCGCGCAGGGGAGGGGCCAGGGGCATCAGT

CBX4-K114R-R: ACTGATGCCCCTGGCCCCTGCGCGCCCAAA

RT-PCR primers:

CBX4-F: ACCGTGCCAAGCTGGATTT

CBX4-R: AGGTCGTACATTTTGGGGTCG

CCL5-F: TGCCCACATCAAGGAGTATTT

CCL5-R: CTTTCGGGTGACAAAGACG

CSNK1G1-F: CCCACAGGTGTATTACTTTGGAC

CSNK1G1-R: GTAAATGTTCGGTCACAGAGGT

CXCL10-F: GGCCATCAAGAATTTACTGAAAGCA

CXCL10-R: TCTGTGTGGTCCATCCTTGGAA

mCXCL10-F: CCAAGTGCTGCCGTCATTTTC

mCXCL10-R: GGCTCGCAGGGATGATTTCAA

mDLOOP1-F: CCCTTCCCCATTTGGTCT

mDLOOP1-R: TGGTTTCACGGAGGATGG

mDLOOP2-F: CCCTTCCCCATTTGGTCT

mDLOOP2-R: TGGTTTCACGGAGGATGG

mGAPDH-F: AGGTCGGTGTGAACGGATTTG

mGAPDH-R: GGGGTCGTTGATGGCAACA

IFI44-F: TTTTCGATGCGAAGATTCACTGG

IFI44-R: CCTGATGCGTTACATGCCCTT

mIFI44-F: ATGCTCCAACTGACTGCTCG

mIFI44-R: ACAGCAATGCCTCTTGTCTTT

IFIT1-F: AGAAGCAGGCAATCACAGAAAA

IFIT1-R: CTGAAACCGACCATAGTGGAAAT

mIFIT1-F: ATCGCGTAGACAAAGCTCTTC

mIFIT1-R: GTTTCGGGATGTCCTCAGTTG

IFNB1-F: ATGACCAACAAGTGTCTCCTCC

IFNB1-R: GGAATCCAAGCAAGTTGTAGCTC

mIFNB1-F: AGCTCCAAGAAAGGACGAACA

mIFNB1-R: AGCTCCAAGAAAGGACGAACA

mISG15-F: GGTGTCCGTGACTAACTCCAT

mISG15-R: CTGTACCACTAGCATCACTGTG

mMX1-F: GACCATAGGGGTCTTGACCAA

mMX1-R: AGACTTGCTCTTTCTGAAAAGCC

OAS1-F: TGTCCAAGGTGGTAAAGGGTG

OAS1-R: CCGGCGATTTAACTGATCCTG

mPLOG1-F: GATGAATGGGCCTACCTTGA

mPLOG1-R: TGGGGTCCTGTTTCTACAGC

SPOP-F: GCCCTCTGCAGTAACCTGTC

SPOP-R: GTCTCCAAGACATCCGAAGC

STING1-F: CACTTGGATGCTTGCCCTC

STING1-R: GCCACGTTGAAATTCCCTTTTT

mTERT-F: CTAGCTCATGTGTCAAGACCCTCTT

mTERT-R: GCCAGCACGTTTCTCTCGTT

U6-qPCR-F: CTCGCTTCGGCAGCACA

U6-qPCR-R: AACGCTTCACGAATTTGCGT

shRNAs, sgRNAs and ISD90

shRNAs were constructed by inserting synthesized oligos into pLKO-puro or pLKO-hygro vector.

shScr: AACAGTCGCGTTTGCGACTGG

shSPOP - A2: CACAGATCAAGGTAGTGAAAT

shSPOP - A3: CAAGGTAGTGAAATTCTCCTA

shSPOP - C4: CAAACGCCTGAAGCAATCCTA

shSPOP - C6: CTCCTACATGTGGACCATCAA

shmSPOP-3: TGTGGACCATCAATAACTTTA

shmSPOP-4: GGAGAGTCAGCGAGCTTATAG

shmSPOP-6: CGCTTGAAGCAATCCTAAGAT

shSTING-29: GCAGAGCTATTTCCTTCCACA

shSTING-45: GTCCAGGACTTGACATCTTAA

shCSNK1G1-1: TGACCGAACATTTACTTTGAA

shCSNK1G1-2: GATGGCAACCTACCTTCGATA

shCSNK1G1-3: GAACCTCATTTACCGAGATGT

shCUL3 - 1: TTCAGGCTTTACAACGTTTAT

shCUL3 - 2: CGTGTGCCAAATGGTTTGAAA

shCBX4-1: GCCCTTCTTTGGGAATATAAT

shCBX4-2: GCCTCAGAGTTCTAGTATTAT

sgRNAs were constructed by inserting synthesized oligos into lentiCRISPRv2-puro vector.

sgSPOP-1: CCTCTGCAGTAACCTGTCCG

sgSPOP-4: TGTCCAAAGAGTGAAGTTC

sgSPOP-11: CCAGTAACAGGTAAAGTGAC

sgSPOP-12: TGTTTGCGAGTAAACCCCAA

sgmSPOP-1: TTCGTGCAAGGCAAAGACTG

sgSTING-1B: GCTGGGACTGCTGTTAAACG

sgmSTING-2: TGCCTCAGATGAGGTCAGTG

sgmSTING-3: TCTTCAGAGCTTGACTCCAG

sgcGAS: GGCCGCCCGTCCGCGCAACT

ISD90:

Immunoblots and immunoprecipitations

Cells were lysed in EBC buffer (50 mM Tris pH 7.5, 120 mM NaCl, 0.5% NP-40) or RIPA buffer (50 mM Tris pH 7.5, 150 mM NaCl, 1% Triton X-100, 1% sodium deoxycholate, 0.1% SDS) supplemented with protease and phosphatase inhibitors (Apexbio, K1008, K1015). Protein concentrations were measured using the Bio-Rad protein assay reagent on a NanoDrop OneC. Equal amounts of lysates were resolved by SDS-PAGE and immunoblotted with indicated antibodies. For immunoprecipitation, 1 mg of lysate was incubated with the indicated antibody (1–2 μg) for 3-4 h at 4 °C, followed by 1 h with 10 μL Protein A/G XPure Agarose Resin (UBPBio, P5030-5). Lysates with tagged proteins were incubated with tag-specific agarose-conjugated antibodies. For endogenous IPs, antibody incubation was performed overnight. Immunocomplexes were washed five times with NETN buffer (20 mM Tris pH 8.0, 100 mM NaCl, 1 mM EDTA, 0.5% NP-40) before SDS-PAGE and immunoblotting. Antibodies used for IB, IP, IF, and FACS are listed in Table S1.

In-cell ubiquitination assays

293T cells were transfected with His–ubiquitin-WT or -K48-only and other indicated construct and treated with 10 μM MG132 (S2619, Selleck) overnight. Cells were lysed in buffer A (6 M guanidine-HCl, 0.1 M Na2HPO4/NaH2PO4, and 10 mM imidazole pH 8.0) and sonicated. Supernatants were incubated with Ni-NTA resins for 3 h at room temperature. Ni-NTA pulldown

products were washed twice with buffer A, twice with buffer A/TI (25% buffer A and 75% buffer TI), and once with buffer TI (25 mM Tris-HCl and 20 mM imidazole pH 6.8). Products were resolved by SDS-PAGE and immunoblotted with indicated antibodies.

Colony formation assays

Cells (500/well) were seeded in 6- or 24-well plates and cultured at 37°C with 5% CO₂ for 7-15 days until visible colonies formed. Colonies were washed with PBS, fixed in methanol for 30 min, and stained with 0.5% crystal violet for 30 min, followed by washing and air drying. Colony numbers were manually counted, and data represent three independent experiments.

RNA extraction and qRT-PCR

RNA was extracted using the RNA Miniprep Super Kit (BS584, BioBasic), and concentration and purity were assessed by NanoDrop OneC (Thermo Fisher Scientific). cDNA was synthesized using the iScript kit (170-8891, Bio-Rad), and qRT-PCR was performed with iTaq SYBR Green Supermix (172-5124, Bio-Rad) on a QuantStudio 6 Flex system. RT² Profiler PCR Arrays for mouse (PAMM-016Z) and human (PAHS-016Z) Type I Interferon Response (Qiagen) were used for RNA profiling. mRNA levels were normalized to GAPDH or U6 snRNA, and relative expression was calculated by the comparative Ct method. Statistical significance was determined by one-way ANOVA. At least 2 biological replicates are included.

Cytosolic DNA isolation and qPCR

B16-OVA cells were treated with or without 10 μ M 6lc for 24 h. Genomic DNA was extracted from half of the cells using QuickExtract DNA Extraction Solution (Bioresearch Technologies,

QE09050). Mitochondria-free cytosolic fractions were isolated from the remaining cells using a Mitochondria Isolation Kit (Thermo Fisher Scientific 89874) per the manufacturer's instructions. Briefly, cell pellets were sequentially treated with reagents A, B, and C, and cytosolic fractions were obtained by centrifugation at 12,000 × g for 15 min. DNA from whole cells and cytosolic fractions was purified using DNA Clean & Concentrator-5 (Zymo Research, D4013) and quantified by NanoDrop. Levels of nuclear and mitochondrial genes in whole-cell DNA were normalized to DNA concentration, and cytosolic DNA levels were further normalized to whole-cell DNA. Statistical significance was determined by one-way ANOVA.

Generation of murine CAR-Ts

Murine T cells were isolated from splenocytes obtained from C57BL/6J mice and stimulated on plates coated with 1 mg/mL of mCD3 and 1 mg/mL of mCD28 mAbs, in complete RPMI 1640 for 48 hrs. Activated murine T cells were transduced with retroviral supernatants using retronectin-coated plates (Takara Bio Inc) with the same protocol used to transduce human T cells with human IL-7/15 (10 ng/mL), as previously described (88). After removal from retronectin plates, T cells were expanded in complete RPMI 1640 medium with human IL-7/15 (10 ng/mL), changing medium every 2 days. On days 7-9, cells were collected and used for functional assays in vivo.

Mouse xenograft assays

B16 cells were transduced with lentiviruses expressing shScr, shmSPOP-6, shmSPOP-3, or shmSPOP-3+HA-SPOP. Two days later, 5-week-old female nude or C57BL/6J mice (Jackson Laboratory; n = 5 per group, 10 injections total) were subcutaneously inoculated with 1×10^5 B16 cells. Tumor dimensions were measured using calipers, and volumes were calculated as $V = L \times 10^5$

 $W^2 \times 0.5$. Mice were euthanized when the largest tumor reached 2,000 mm³, and tumors were excised and weighed.

For combination therapy studies, 1×10⁵ B16 cells (parental, sgCtrl, or sgSTING) were injected subcutaneously into the right flank of 5-week-old female C57BL/6J mice. When tumors became palpable (~day 7), mice were randomized into four treatment groups. Compound 6b (8 mg/ml in 10% DMSO, 40% PEG300, 5% Tween-80, and 45% saline) was administered intraperitoneally at 60 mg/kg daily, 6lc at 20 mg/kg daily, and anti–PD-1 antibody (BE0273, BioXCell) at 250 μg intraperitoneally every three days. Tumor growth was monitored as above, and tumors were collected at endpoint for flow cytometry analysis of infiltrating immune cells.

Comet assay

Single-strand DNA breaks were assessed using a Comet assay as previously described (44). B16 cells were treated with 10 μ M 6b for 24 h. Low-gelling agarose (0.5% and 1.5%, A4018, Sigma) was prepared, and slides were pre-coated with 1.5% agarose. Cells (10⁴ per slide) were mixed with 0.5% agarose, layered onto pre-coated slides, and gelled at 4 °C for 2 min. Slides were lysed overnight at 4 °C in lysis solution (2.5 M NaCl, 100 mM EDTA, 10 mM Tris-HCl pH 7.5, 200 mM NaOH, 1% Triton X-100, 10% DMSO) in the dark, then equilibrated in electrophoresis solution (300 mM NaOH, 1 mM EDTA, pH 13) and subjected to electrophoresis at 25 V, 300 mA for 25 min. Slides were neutralized with 0.4 M Tris-HCl (pH 8.0), stained with propidium iodide (10 μ g/mL), and washed with water. At least 50 comet images per condition were captured at ×20 magnification (Olympus IX51). Tail moment was quantified as: tail length × tail intensity / comet intensity.

K-ε-GG peptides enrichment and LC-MS/MS

A2058 cells stably expressing shScramble or shSPOP-C4 were treated with or without 10 μM 6lc for 12 h (n = 3 per group). Cells were washed with PBS, lysed in heated 5% SDS/50 mM TEAB (pH 7.55) with 5 mM TCEP at 95 °C, sonicated, and alkylated with 15 mM MMTS for 30 min. Proteins were quantified using the Bio-Rad assay, and digested using S-Trap Midi columns (UNC Proteomics Core). Peptides were quantified with the Pierce fluorometric assay; 820 μg per sample was processed, and a pooled aliquot was used for QC. Approximately 800 μg per sample underwent K-ε-GG enrichment using the PTMScan HS Ubiquitin Remnant Motif Kit (59322, Cell Signaling Technology); 2% input was reserved for proteome analysis. Samples were desalted and analyzed by LC-MS/MS (Ultimate3000-Exploris480; proteome: 130 min DIA; K-ε-GG: 100 min DIA). Data were analyzed in Spectronaut (v17.1) using the UniProt Human (reviewed, Jan 2023) and MaxQuant contaminant databases. Single-peptide identifications were excluded from proteome data; imputation and cross-run normalization were applied. For K-ε-GG data, digly-Lys was set as a variable modification, cross-run normalization was enabled, and no imputation was performed. Statistical analyses were conducted in Spectronaut.

Flow cytometry

To analyze tumor-infiltrating immune cells, B16 tumors were digested using tumor dissociation kit, mouse (130-096-730, Miltenyi Biotec) and gentleMACS Dissociator according to the protocols by Miltenyi Biotec. Single cell suspension was incubated with corresponding fluorophore conjugated antibodies and isotype controls. Samples were acquired on a Symphony A3or Fortessa flow cytometer from BD. Data was analyzed using Flowjo 10.8.1.

Single cell RNA-Seq analysis

Harvesting the B16-bearing mice at day 14. The Single-cell RNA-Seq was done as previously described (61). In brief, tumor-infiltrating CD45+ cells were enriched through positive selection via anti-CD45 biotinylated antibody and streptavidin-labeled microbeads and Miltenyi MACS LS columns. Then PE-CD45+ cells were sorted on a SONY XYZ instrument, and 10000 cells were loaded in 10x Genomics Chromium Single Cell 3' inlets (one inlet per sample). Barcoding and library preparation were performed following manufacture instructions with the 10x Genomics Chromium GEM-X Single Cell 3' kit v4. Sequencing was performed on a Illumina NextSeq 2000 at the UNC High throughput Sequencing Facility. Sequencing reads were mapped to mm10, and unique molecular identifier (UMI) counts were collapsed based on the 10x Genomics Cell Ranger software (version 8.0.1). Resulting datasets were analyzed via the Seurat package (v5.1.0) in R (v4.3.1). Raw counts were processed following standard quality control measures and low-quality cells were excluded, including dead and suspected doublets. The minimum number of principal components needed to represent the data were calculated using a Jack Straw Plot, and next clustering was performed at a resolution of 0.7.

Immunofluorescence

Cells plated onto glass coverslips were fixed with 4% paraformaldehyde in PBS for 20 min at room temperature and permeabilized with 0.2% Triton X-100 for 20 min at room temperature. Cells were incubated with blocking buffer (5% bovine serum albumin and 0.1% Triton X-100 in PBS) for 1 hr, incubated with primary antibodies at 4 °C overnight, incubated with secondary antibodies at room temperature for 1 hr and mounted with ProLong Gold antifade reagent (P36931,

Invitrogen). Fluorescent signals were observed with an Olympus FV1000 confocal microscope at $60\times$ or $100\times$ magnification.

Immunohistochemical (IHC) analysis

Freshly isolated B16 tumors from C57BL/6 mice were fixed in 10% neutral-buffered formalin for 48 h, transferred to cassettes, stored in 70% ethanol, embedded in paraffin, and sectioned into five consecutive 6-µm slices. For IHC, slides were deparaffinized in xylene (2 × 10 min), rehydrated through graded ethanol (100%, 95%, 85%, 70%), and rinsed in TBST (15 min) followed by TBS (5 min). Endogenous peroxidase activity was quenched with 1% hydrogen peroxide in methanol (10 min). Antigen retrieval was performed by microwaving slides in 0.01 M sodium citrate buffer (pH 6.0, 0.05% Tween-20) for 5 min at full power and 10 min at 50% power, then cooling for 30 min. After TBS washes (3 × 3 min), sections were blocked in buffer (10 mM Tris-HCl, 0.1 M MgCl₂, 0.5% Tween-20, 1% BSA, 10% goat serum) for 1 h at room temperature. Primary antibodies diluted in 2% BSA/PBS were applied overnight at 4°C. Slides were washed and incubated with a biotinylated secondary antibody (1:400, Vector Labs) for 1 h, then with avidinbiotin complex (ABC reagent, Vector Labs) for 45 min. Chromogenic detection was performed with freshly prepared DAB substrate (Vector Labs) for optimized times (CD3ε, 3 min; CD8α, 5 min; FoxP3, 3 min; STING, 1 min; PD-L1, 4 min). Reactions were stopped in running tap water. Slides were counterstained with diluted Harris hematoxylin (2 min), dehydrated through graded ethanols and xylene, and mounted with Permount.

Protein purification

His-CBX4 and His-SUMO-avi-SPOP (28–359 aa) were expressed in *E. coli* BL21 (DE3) CodonPlus-RIL cells grown in LB with kanamycin (50 μg/mL)-CBX4, ampicillin (150 μg/mL)-SPOP, and chloramphenicol (30 μg/mL) at 37 °C to OD₆₀₀ = 0.8, followed by induction with 0.6 mM IPTG at 16 °C for 18 h. Cells were lysed in buffer (50 mM HEPES pH 7.5, 200 mM NaCl, 20 mM imidazole pH 8.0, 5 mM BME, 0.001% PMSF) by sonication, and lysates were clarified at 17,500 rpm for 45 min. Proteins were purified using Ni-NTA resin (R-202-100, GoldBio), and dialyzed (3.5 kD cutoff) overnight (50 mM HEPES pH 7.5, 200 mM NaCl, 2 mM DTT). His-CBX4 was stored after dialysis. Avi-SPOP was cleaved from SUMO using ULP1 (1:50) during dialysis, further purified by size-exclusion chromatography (20 mM HEPES pH 8.0, 200 mM NaCl, 1 mM DTT), and biotinylated with biotin maleimide.

Streptavidin pulldown

Dynabeads MyOne Streptavidin T1 (10 μ L; 65602, Thermo Fisher Scientific) were washed twice with NETN buffer before use. Beads were incubated with 1 μ M biotin-SPOP or D-(+)-biotin (ALX-460-002-G001, Enzo) in 100 μ L buffer for 1 hour and washed once with NETN to remove unbound biotin. The beads were then incubated with the indicated concentrations of SPOP inhibitors for 30 minutes, followed by incubation with 0.5 μ M CBX4 for 1 hour. After four washes with NETN buffer, bound proteins were eluted, separated by SDS-PAGE, and immunoblotted with the indicated antibodies.

Statistical Analysis

Statistical analyses were performed using GraphPad Prism 8. Two-group comparisons used two-tailed unpaired Student's t-tests. For three or more groups, normally distributed data were analyzed

by one- or two-way ANOVA with Dunnett's, Tukey's, Fisher's LSD, or Bonferroni post hoc tests as appropriate; non-normally distributed data used Kruskal-Wallis with Dunn's test. Results are shown as mean \pm SD from representative experiments repeated at least twice, or as mean \pm SEM from at least two independent experiments or biological replicates.

Study approval

All mouse studies were reviewed and approved by the UNC Institutional Animal Care and Use Committee (IACUC#22-056, #23-192, and #25-017.0). Experiments were conducted in the Genetic Medicine Animal Facility at UNC-Chapel Hill, an Office of Laboratory Animal Welfare—assured and AAALAC-accredited facility, following IACUC-approved protocols and in compliance with the Guide for the Care and Use of Laboratory Animals (National Research Council, 2011).

Data availability

Data availability. All reported data values are available in the Supporting Data Values file. scRNA-Seq data supporting the findings in this study has been deposited in GEO for public accesses (GSE280269). All other data supporting the findings in this study are available from the corresponding authors upon reasonable request.

References:

- 1. Scheffner M, Nuber U, and Huibregtse JM. Protein ubiquitination involving an E1-E2-E3 enzyme ubiquitin thioester cascade. *Nature*. 1995;373(6509):81-3.
- 2. Li C, Ao J, Fu J, Lee DF, Xu J, Lonard D, et al. Tumor-suppressor role for the SPOP ubiquitin ligase in signal-dependent proteolysis of the oncogenic co-activator SRC-3/AIB1. *Oncogene*. 2011;30(42):4350-64.
- 3. Theurillat JP, Udeshi ND, Errington WJ, Svinkina T, Baca SC, Pop M, et al. Prostate cancer. Ubiquitylome analysis identifies dysregulation of effector substrates in SPOP-mutant prostate cancer. *Science*. 2014;346(6205):85-9.
- 4. Ma J, Chang K, Peng J, Shi Q, Gan H, Gao K, et al. SPOP promotes ATF2 ubiquitination and degradation to suppress prostate cancer progression. *J Exp Clin Cancer Res.* 2018;37(1):145.
- 5. An J, Ren S, Murphy SJ, Dalangood S, Chang C, Pang X, et al. Truncated ERG Oncoproteins from TMPRSS2-ERG Fusions Are Resistant to SPOP-Mediated Proteasome Degradation. *Mol Cell.* 2015;59(6):904-16.
- 6. Gan W, Dai X, Lunardi A, Li Z, Inuzuka H, Liu P, et al. SPOP Promotes Ubiquitination and Degradation of the ERG Oncoprotein to Suppress Prostate Cancer Progression. *Mol Cell*. 2015;59(6):917-30.
- 7. Su S, Chen J, Jiang Y, Wang Y, Vital T, Zhang J, et al. SPOP and OTUD7A Control EWS-FLI1 Protein Stability to Govern Ewing Sarcoma Growth. *Adv Sci (Weinh)*. 2021;8(14):e2004846.
- 8. Dai X, Gan W, Li X, Wang S, Zhang W, Huang L, et al. Prostate cancer-associated SPOP mutations confer resistance to BET inhibitors through stabilization of BRD4. *Nat Med.* 2017;23(9):1063-71.
- 9. Zhang P, Wang D, Zhao Y, Ren S, Gao K, Ye Z, et al. Intrinsic BET inhibitor resistance in SPOP-mutated prostate cancer is mediated by BET protein stabilization and AKT-mTORC1 activation. *Nat Med.* 2017;23(9):1055-62.
- 10. Li G, Ci W, Karmakar S, Chen K, Dhar R, Fan Z, et al. SPOP promotes tumorigenesis by acting as a key regulatory hub in kidney cancer. *Cancer Cell.* 2014;25(4):455-68.
- 11. An J, Wang C, Deng Y, Yu L, and Huang H. Destruction of full-length androgen receptor by wild-type SPOP, but not prostate-cancer-associated mutants. *Cell Rep.* 2014;6(4):657-69.
- 12. Wu F, Dai X, Gan W, Wan L, Li M, Mitsiades N, et al. Prostate cancer-associated mutation in SPOP impairs its ability to target Cdc20 for poly-ubiquitination and degradation. *Cancer Lett.* 2017;385:207-14.
- 13. Ju LG, Zhu Y, Long QY, Li XJ, Lin X, Tang SB, et al. SPOP suppresses prostate cancer through regulation of CYCLIN E1 stability. *Cell Death Differ*. 2019;26(6):1156-68.
- 14. Jin X, Qing S, Li Q, Zhuang H, Shen L, Li J, et al. Prostate cancer-associated SPOP mutations lead to genomic instability through disruption of the SPOP-HIPK2 axis. *Nucleic Acids Res.* 2021;49(12):6788-803.
- 15. Wang D, Ma J, Botuyan MV, Cui G, Yan Y, Ding D, et al. ATM-phosphorylated SPOP contributes to 53BP1 exclusion from chromatin during DNA replication. *Sci Adv.* 2021;7(25).
- 16. Wang Z, Li L, Ye Q, Lei Y, Lu M, Ye L, et al. Cancer-associated SPOP mutations enlarge nuclear size and facilitate nuclear envelope rupture upon farnesyltransferase inhibitor treatment. *J Clin Invest.* 2025;135(14).
- 17. Su S, Chen J, Wang Y, Wong LM, Zhu Z, Jiang G, et al. Lenalidomide downregulates ACE2 protein abundance to alleviate infection by SARS-CoV-2 spike protein conditioned pseudoviruses. *Signal Transduct Target Ther.* 2021;6(1):182.

- 18. Geng C, Zhang MC, Manyam GC, Vykoukal JV, Fahrmann JF, Peng S, et al. SPOP Mutations Target STING1 Signaling in Prostate Cancer and Create Therapeutic Vulnerabilities to PARP Inhibitor-Induced Growth Suppression. *Clin Cancer Res.* 2023;29(21):4464-78.
- 19. Wang L, Lin M, Chu M, Liu Y, Ma J, He Y, et al. SPOP promotes ubiquitination and degradation of LATS1 to enhance kidney cancer progression. *EBioMedicine*. 2020;56:102795.
- 20. Hu YH, Wang Y, Wang F, Dong YM, Jiang WL, Wang YP, et al. SPOP negatively regulates Toll-like receptor-induced inflammation by disrupting MyD88 self-association. *Cell Mol Immunol.* 2021;18(7):1708-17.
- 21. Jin X, Shi Q, Li Q, Zhou L, Wang J, Jiang L, et al. CRL3-SPOP ubiquitin ligase complex suppresses the growth of diffuse large B-cell lymphoma by negatively regulating the MyD88/NF-kappaB signaling. *Leukemia*. 2020;34(5):1305-14.
- 22. Li Q, Wang F, Wang Q, Zhang N, Zheng J, Zheng M, et al. SPOP promotes ubiquitination and degradation of MyD88 to suppress the innate immune response. *PLoS Pathog.* 2020;16(5):e1008188.
- 23. Gao K, Shi Q, Gu Y, Yang W, He Y, Lv Z, et al. SPOP mutations promote tumor immune escape in endometrial cancer via the IRF1-PD-L1 axis. *Cell Death Differ*. 2023;30(2):475-87.
- 24. Zhang J, Bu X, Wang H, Zhu Y, Geng Y, Nihira NT, et al. Cyclin D-CDK4 kinase destabilizes PD-L1 via cullin 3-SPOP to control cancer immune surveillance. *Nature*. 2018;553(7686):91-5.
- 25. Dong M, Qian M, and Ruan Z. CUL3/SPOP complex prevents immune escape and enhances chemotherapy sensitivity of ovarian cancer cells through degradation of PD-L1 protein. *J Immunother Cancer*. 2022;10(10).
- 26. Boukhaled GM, Harding S, and Brooks DG. Opposing Roles of Type I Interferons in Cancer Immunity. *Annu Rev Pathol.* 2021;16:167-98.
- 27. Yu R, Zhu B, and Chen D. Type I interferon-mediated tumor immunity and its role in immunotherapy. *Cell Mol Life Sci.* 2022;79(3):191.
- 28. Deng Y, Wang Y, Li L, Miao EA, and Liu P. Post-Translational Modifications of Proteins in Cytosolic Nucleic Acid Sensing Signaling Pathways. *Front Immunol.* 2022;13:898724.
- 29. Sun L, Wu J, Du F, Chen X, and Chen ZJ. Cyclic GMP-AMP synthase is a cytosolic DNA sensor that activates the type I interferon pathway. *Science*. 2013;339(6121):786-91.
- 30. Wu J, Sun L, Chen X, Du F, Shi H, Chen C, et al. Cyclic GMP-AMP is an endogenous second messenger in innate immune signaling by cytosolic DNA. *Science*. 2013;339(6121):826-30.
- 31. Ishikawa H, and Barber GN. STING is an endoplasmic reticulum adaptor that facilitates innate immune signalling. *Nature*. 2008;455(7213):674-8.
- 32. Yu L, and Liu P. Cytosolic DNA sensing by cGAS: regulation, function, and human diseases. *Signal Transduct Target Ther.* 2021;6(1):170.
- 33. Ramanjulu JM, Pesiridis GS, Yang J, Concha N, Singhaus R, Zhang SY, et al. Design of amidobenzimidazole STING receptor agonists with systemic activity. *Nature*. 2018;564(7736):439-43.
- 34. Ma M, Dang Y, Chang B, Wang F, Xu J, Chen L, et al. TAK1 is an essential kinase for STING trafficking. *Mol Cell*. 2023;83(21):3885-903 e5.
- 35. Wang Z, Liu P, Inuzuka H, and Wei W. Roles of F-box proteins in cancer. *Nat Rev Cancer*. 2014;14(4):233-47.
- 36. Sackton KL, Dimova N, Zeng X, Tian W, Zhang M, Sackton TB, et al. Synergistic blockade of mitotic exit by two chemical inhibitors of the APC/C. *Nature*. 2014;514(7524):646-9.

- 37. Wu L, Grigoryan AV, Li Y, Hao B, Pagano M, and Cardozo TJ. Specific small molecule inhibitors of Skp2-mediated p27 degradation. *Chem Biol.* 2012;19(12):1515-24.
- 38. Chan CH, Morrow JK, Li CF, Gao Y, Jin G, Moten A, et al. Pharmacological inactivation of Skp2 SCF ubiquitin ligase restricts cancer stem cell traits and cancer progression. *Cell*. 2013;154(3):556-68.
- 39. Shen H, and Maki CG. Pharmacologic activation of p53 by small-molecule MDM2 antagonists. *Curr Pharm Des.* 2011;17(6):560-8.
- 40. Li ASM, Kimani S, Wilson B, Noureldin M, Gonzalez-Alvarez H, Mamai A, et al. Discovery of Nanomolar DCAF1 Small Molecule Ligands. *J Med Chem.* 2023;66(7):5041-60.
- 41. Guo ZQ, Zheng T, Chen B, Luo C, Ouyang S, Gong S, et al. Small-Molecule Targeting of E3 Ligase Adaptor SPOP in Kidney Cancer. *Cancer Cell*. 2016;30(3):474-84.
- 42. Dong Z, Wang Z, Guo ZQ, Gong S, Zhang T, Liu J, et al. Structure-Activity Relationship of SPOP Inhibitors against Kidney Cancer. *J Med Chem.* 2020;63(9):4849-66.
- 43. Gonugunta VK, Sakai T, Pokatayev V, Yang K, Wu J, Dobbs N, et al. Trafficking-Mediated STING Degradation Requires Sorting to Acidified Endolysosomes and Can Be Targeted to Enhance Anti-tumor Response. *Cell Rep.* 2017;21(11):3234-42.
- 44. Olive PL, and Banath JP. The comet assay: a method to measure DNA damage in individual cells. *Nat Protoc*. 2006;1(1):23-9.
- 45. Zhou L, Zhang YF, Yang FH, Mao HQ, Chen Z, and Zhang L. Mitochondrial DNA leakage induces odontoblast inflammation via the cGAS-STING pathway. *Cell Commun Signal*. 2021;19(1):58.
- 46. Sievers QL, Petzold G, Bunker RD, Renneville A, Slabicki M, Liddicoat BJ, et al. Defining the human C2H2 zinc finger degrome targeted by thalidomide analogs through CRBN. *Science*. 2018;362(6414).
- 47. Lu G, Middleton RE, Sun H, Naniong M, Ott CJ, Mitsiades CS, et al. The myeloma drug lenalidomide promotes the cereblon-dependent destruction of Ikaros proteins. *Science*. 2014;343(6168):305-9.
- 48. Kronke J, Udeshi ND, Narla A, Grauman P, Hurst SN, McConkey M, et al. Lenalidomide causes selective degradation of IKZF1 and IKZF3 in multiple myeloma cells. *Science*. 2014;343(6168):301-5.
- 49. Ito T, and Handa H. Cereblon and its downstream substrates as molecular targets of immunomodulatory drugs. *Int J Hematol.* 2016;104(3):293-9.
- 50. Di Croce L, and Helin K. Transcriptional regulation by Polycomb group proteins. *Nat Struct Mol Biol.* 2013;20(10):1147-55.
- 51. Zeng JS, Zhang ZD, Pei L, Bai ZZ, Yang Y, Yang H, et al. CBX4 exhibits oncogenic activities in breast cancer via Notch1 signaling. *Int J Biochem Cell Biol*. 2018;95:1-8.
- 52. Hu C, Zhang Q, Tang Q, Zhou H, Liu W, Huang J, et al. CBX4 promotes the proliferation and metastasis via regulating BMI-1 in lung cancer. *J Cell Mol Med.* 2020;24(1):618-31.
- 53. Chen F, Hou W, Yu X, Wu J, Li Z, Xu J, et al. CBX4 deletion promotes tumorigenesis under Kras(G12D) background by inducing genomic instability. *Signal Transduct Target Ther.* 2023;8(1):343.
- 54. Ismail IH, Gagne JP, Caron MC, McDonald D, Xu Z, Masson JY, et al. CBX4-mediated SUMO modification regulates BMI1 recruitment at sites of DNA damage. *Nucleic Acids Res.* 2012;40(12):5497-510.
- 55. Fitieh A, Locke AJ, Mashayekhi F, Khaliqdina F, Sharma AK, and Ismail IH. BMI-1 regulates DNA end resection and homologous recombination repair. *Cell Rep.* 2022;38(12):110536.

- 56. Jacquelot N, Roberti MP, Enot DP, Rusakiewicz S, Ternes N, Jegou S, et al. Predictors of responses to immune checkpoint blockade in advanced melanoma. *Nat Commun*. 2017;8(1):592.
- 57. Auslander N, Zhang G, Lee JS, Frederick DT, Miao B, Moll T, et al. Robust prediction of response to immune checkpoint blockade therapy in metastatic melanoma. *Nat Med*. 2018;24(10):1545-9.
- 58. Maibach F, Sadozai H, Seyed Jafari SM, Hunger RE, and Schenk M. Tumor-Infiltrating Lymphocytes and Their Prognostic Value in Cutaneous Melanoma. *Front Immunol*. 2020;11:2105.
- 59. Reislander T, Groelly FJ, and Tarsounas M. DNA Damage and Cancer Immunotherapy: A STING in the Tale. *Mol Cell*. 2020;80(1):21-8.
- 60. Meng X, Liu X, Guo X, Jiang S, Chen T, Hu Z, et al. FBXO38 mediates PD-1 ubiquitination and regulates anti-tumour immunity of T cells. *Nature*. 2018;564(7734):130-5.
- 61. Zhou X, Wang Y, Dou Z, Delfanti G, Tsahouridis O, Pellegry CM, et al. CAR-redirected natural killer T cells demonstrate superior antitumor activity to CAR-T cells through multimodal CD1d-dependent mechanisms. *Nat Cancer.* 2024.
- 62. Hollern DP, Xu N, Thennavan A, Glodowski C, Garcia-Recio S, Mott KR, et al. B Cells and T Follicular Helper Cells Mediate Response to Checkpoint Inhibitors in High Mutation Burden Mouse Models of Breast Cancer. *Cell.* 2019;179(5):1191-206 e21.
- 63. Zhang H, Liu L, Liu J, Dang P, Hu S, Yuan W, et al. Roles of tumor-associated macrophages in anti-PD-1/PD-L1 immunotherapy for solid cancers. *Mol Cancer*. 2023;22(1):58.
- 64. Takeuchi Y, Tanemura A, Tada Y, Katayama I, Kumanogoh A, and Nishikawa H. Clinical response to PD-1 blockade correlates with a sub-fraction of peripheral central memory CD4+ T cells in patients with malignant melanoma. *Int Immunol.* 2018;30(1):13-22.
- 65. Nguyen NT, Huang K, Zeng H, Jing J, Wang R, Fang S, et al. Nano-optogenetic engineering of CAR T cells for precision immunotherapy with enhanced safety. *Nat Nanotechnol*. 2021;16(12):1424-34.
- 66. Chen J, Lopez-Moyado IF, Seo H, Lio CJ, Hempleman LJ, Sekiya T, et al. NR4A transcription factors limit CAR T cell function in solid tumours. *Nature*. 2019;567(7749):530-4.
- 67. Owen K, Ghaly R, Shohdy KS, and Thistlethwaite F. Lymphodepleting chemotherapy practices and effect on safety and efficacy outcomes in patients with solid tumours undergoing T cell receptor-engineered T cell (TCR-T) Therapy: a systematic review and meta-analysis. *Cancer Immunol Immunother.* 2023;72(4):805-14.
- 68. Dong G, Ding Y, He S, and Sheng C. Molecular Glues for Targeted Protein Degradation: From Serendipity to Rational Discovery. *J Med Chem.* 2021;64(15):10606-20.
- 69. Sakamoto KM, Kim KB, Kumagai A, Mercurio F, Crews CM, and Deshaies RJ. Protacs: chimeric molecules that target proteins to the Skp1-Cullin-F box complex for ubiquitination and degradation. *Proc Natl Acad Sci U S A*. 2001;98(15):8554-9.
- 70. Uehara T, Minoshima Y, Sagane K, Sugi NH, Mitsuhashi KO, Yamamoto N, et al. Selective degradation of splicing factor CAPERalpha by anticancer sulfonamides. *Nat Chem Biol.* 2017;13(6):675-80.
- 71. Han T, Goralski M, Gaskill N, Capota E, Kim J, Ting TC, et al. Anticancer sulfonamides target splicing by inducing RBM39 degradation via recruitment to DCAF15. *Science*. 2017;356(6336).

- 72. Slabicki M, Kozicka Z, Petzold G, Li YD, Manojkumar M, Bunker RD, et al. The CDK inhibitor CR8 acts as a molecular glue degrader that depletes cyclin K. *Nature*. 2020;585(7824):293-7.
- 73. Mayor-Ruiz C, Bauer S, Brand M, Kozicka Z, Siklos M, Imrichova H, et al. Rational discovery of molecular glue degraders via scalable chemical profiling. *Nat Chem Biol.* 2020;16(11):1199-207.
- 74. Lv L, Chen P, Cao L, Li Y, Zeng Z, Cui Y, et al. Discovery of a molecular glue promoting CDK12-DDB1 interaction to trigger cyclin K degradation. *Elife*. 2020;9.
- 75. Simonetta KR, Taygerly J, Boyle K, Basham SE, Padovani C, Lou Y, et al. Prospective discovery of small molecule enhancers of an E3 ligase-substrate interaction. *Nat Commun*. 2019;10(1):1402.
- 76. Wang H, Hu S, Chen X, Shi H, Chen C, Sun L, et al. cGAS is essential for the antitumor effect of immune checkpoint blockade. *Proc Natl Acad Sci U S A*. 2017;114(7):1637-42.
- 77. Hugo W, Zaretsky JM, Sun L, Song C, Moreno BH, Hu-Lieskovan S, et al. Genomic and Transcriptomic Features of Response to Anti-PD-1 Therapy in Metastatic Melanoma. *Cell*. 2016;165(1):35-44.
- 78. Gellrich FF, Schmitz M, Beissert S, and Meier F. Anti-PD-1 and Novel Combinations in the Treatment of Melanoma-An Update. *J Clin Med.* 2020;9(1).
- 79. Kennedy R, and Celis E. Multiple roles for CD4+ T cells in anti-tumor immune responses. *Immunol Rev.* 2008;222:129-44.
- 80. Gnjatic S, Atanackovic D, Jager E, Matsuo M, Selvakumar A, Altorki NK, et al. Survey of naturally occurring CD4+ T cell responses against NY-ESO-1 in cancer patients: correlation with antibody responses. *Proc Natl Acad Sci U S A*. 2003;100(15):8862-7.
- 81. Reed CM, Cresce ND, Mauldin IS, Slingluff CL, Jr., and Olson WC. Vaccination with Melanoma Helper Peptides Induces Antibody Responses Associated with Improved Overall Survival. *Clin Cancer Res.* 2015;21(17):3879-87.
- 82. Kruse B, Buzzai AC, Shridhar N, Braun AD, Gellert S, Knauth K, et al. CD4(+) T cell-induced inflammatory cell death controls immune-evasive tumours. *Nature*. 2023;618(7967):1033-40.
- 83. Jiang Y, Zhang Y, Leung JY, Fan C, Popov KI, Su S, et al. MERTK mediated novel site Akt phosphorylation alleviates SAV1 suppression. *Nat Commun.* 2019;10(1):1515.
- 84. Liu P, Begley M, Michowski W, Inuzuka H, Ginzberg M, Gao D, et al. Cell-cycle-regulated activation of Akt kinase by phosphorylation at its carboxyl terminus. *Nature*. 2014;508(7497):541-5.
- 85. Zhang Y, Ma Z, Wang Y, Boyer J, Ni G, Cheng L, et al. Streptavidin Promotes DNA Binding and Activation of cGAS to Enhance Innate Immunity. *iScience*. 2020;23(9):101463.
- 86. Liu P, Gan W, Su S, Hauenstein AV, Fu TM, Brasher B, et al. K63-linked polyubiquitin chains bind to DNA to facilitate DNA damage repair. *Sci Signal*. 2018;11(533).
- 87. Liu J, Wan L, Liu P, Inuzuka H, Liu J, Wang Z, et al. SCF(beta-TRCP)-mediated degradation of NEDD4 inhibits tumorigenesis through modulating the PTEN/Akt signaling pathway. *Oncotarget*. 2014;5(4):1026-37.
- 88. Dou Z, Bonacci TR, Shou P, Landoni E, Woodcock MG, Sun C, et al. 4-1BB-encoding CAR causes cell death via sequestration of the ubiquitin-modifying enzyme A20. *Cell Mol Immunol*. 2024;21(8):905-17.

Acknowledgments: Animal studies were performed within the UNC Lineberger Animal Study Core at the University of North Carolina at Chapel Hill, which is supported in part by an NCI Center Core Support Grant (CA16086) to the UNC Lineberger Comprehensive Cancer Center. Figures 1A, 4J, 6H, 9A, 9B and 11L were created by BioRender. We thank Dr. Deborah DeRyckere (Emory University) for kindly sharing human melanoma cell lines used in this study. We also thank Dr. Virginia Byers Kraus (Duke University) for kindly sharing the CBX4 cDNA. This work was supported by a National Institutes of Health grant R01CA244825 (PL), a DoD CDMRP KCRP IDA grant HT9425-24-1-0644 (PL) and The University of North Carolina at Chapel Hill University Cancer Research Fund (PL).

Author contributions: Conceptualization: GD, PL; Methodology: ZZ, XZ, GD, PL, MGW, LEH; Investigation: ZZ, XZ, MX, JC, KCR, ACM; Visualization: ZZ, XZ, GA, MGW, LEH, GD, PL; Funding acquisition: PL; Project administration: GD, PL; Supervision: GD, PL; Writing – original draft: ZZ, XZ, PL.

Figure Legends

Figure 1. SPOP depletion suppresses B16 tumor growth depending on tumor immune environment. (A) Xenograft schema. Tumor volume and weight in nude mice and C57BL/6J mice injected with B16 cells expressing shScr and shmSPOP-6 were measured. (B) Tumor volume measurements over time for xenograft of indicated B16 cell lines. Error bars represent SEM, n = 10. (C) Isolated tumors from (B) and weighed in (D) Error bars represent SEM, n = 10. (E) Immunoblot (IB) analyses of control, SPOP depleted and reconstituted B16 cells. (F) Tumor volume measurements over time for xenograft of B16 cells in (E). Error bars represent SEM, n = 14. (G) Isolated tumors from (F) and weighed in (H) Error bars represent SEM, n = 14. *P* values were calculated using two-way ANOVA followed by Tukey's multiple comparison test (B and F), two-tailed unpaired Student's t test (D), or one-way ANOVA followed by Fisher's LSD multiple comparison test (H). Representative experiments shown in figures were repeated at least two times independently with similar results.

Figure 2. SPOP depletion potentiates type I interferon response. (A) IB analyses of control and SPOP depleted A2058 cells. (B) RNA expression profiling heatmap of genes in human type-I interferon response in A2058 cells from (A). (C) RT-PCR analyses of mRNA changes in A2058 cells from (A). Error bars represent SD, n = 3. *p < 0.05 (two-tailed unpaired Student's t test). (D) IB analysis of indicated HMCB cells treated with 5 μ g/mL 2'3-cGAMP for indicated hours.

Figure 3. SPOP targets STING for ubiquitination and degradation. (A to C) IB analyses of indicated cells depleted of SPOP by shRNAs or sgRNAs. (D to G) IB analyses of indicated cells

depleted of SPOP and rescued by stably expressing shRNA/sgRNA-resistant SPOP. (H) IB analyses of indicated cells transfected with HA-SPOP construct. (I) IB analyses of 293T cells treated with 10 μM of MG132 overnight after transfecting with indicated constructs for 36 hrs. (J) IB analysis of control and SPOP depleted A2058 cells treated with 100 μg/mL of cycloheximide (CHX) for indicated periods. (K) Quantification of relative STING grayscales in (J). (L) Schematic illustration of potential SPOP-binding motifs in human and mouse STING and corresponding mutations. (M) IB analyses of HA-IP and WCL derived from 293T cells transfected with indicated constructs. (N) IB analyses of Flag-IP and WCL derived from B16 cells stably expressing indicated molecules by lentivirus infection. (O) IB analyses of WCL and Ni-NTA pulldown products derived from 293T cells transfected with the indicated constructs. Cells in (L to N) were treated with 10 μM of MG132 overnight before collection. Representative experiments shown in figures were repeated at least two times independently with similar results.

Figure 4. CK1γ1 phosphorylates STING for SPOP-mediated ubiquitination and degradation.

(A) IB analyses of 293T cells co-transfected with constructs of Flag-STING and Myc-tagged casein kinases. (B) IB analyses of Flag-IP and WCL derived from 293T cells transfected with indicated constructs and overnight treated with 20 nM of Baf-A1. (C) IB analyses of indicated cells depleted of CK1 γ 1. (D and E) RT-PCR analyses of mRNA changes in 786-o cells depleted of CK1 γ 1. Error bars represent SD, n = 2. *p < 0.05 compared with shScr (one-way ANOVA followed by Dunnett's multiple comparison test). (F) IB analyses of 293T overnight treated with 10 μ M of MG132, 1 μ M of MLN4294 and 20 nM of Baf-A1 after transfecting with indicated constructs for 36 hrs. (G) IB analyses of 293T cells transfected with indicated constructs. (H and I) IB analyses of indicated cells treated with indicated doses of D4476 (H) and epiblastin A (I) for

24 hrs. **J**, Schematic of STING degradation triggered by SPOP and CK1γ1. Representative experiments shown in figures were repeated at least two times independently with similar results.

Figure 5. Evading SPOP-mediated degradation enhances STING activation in innate immunity. (A) IB analyses of indicated 786-o stable cell lines treated with 5 μ g/mL of ISD90 for indicated periods. (B to C) RT-PCR analyses of indicated 786-o stable cell lines treated with 5 μ g/mL of ISD90 (b) or 3 μ M of diABZI (c) for indicated periods. Error bars represent SD, n = 3. (D) Schematic illustration of patient STING-T356M mutation in the SPOP-binding motif. (E) IB analyses of HA-IP and WCL derived from 293T cells transfected with indicated constructs. (F) IB analyses of WCL and Ni–NTA pulldown products derived from 293T cells transfected with the indicated constructs. Cells in (E and F) were treated with 10 μ M of MG132 overnight before collection. (G) IB analyses of 293T cells transfected with fixed dose of STING constructs and increased dose of SPOP construct. (H) IB analysis of Flag-STING-WT and -T356M-reconstituting 786-o cells treated with 100 μ g/ml of CHX for indicated periods. (I) Quantification of relative Flag grayscales in (H). Error bars represent SEM, n = 2. One-way ANOVA followed by Tukey's multiple comparison test (B, C), two-way ANOVA (I). *p < 0.05. Representative experiments shown in figures were repeated at least two times independently with similar results.

Figure 6. The STING-T356M mutant exhibits an enhanced ability to respond to dsDNA, owing to its evasion of SPOP-mediated degradation. (A and B) IB analyses (A) and RT-PCR analyses (B) of indicated 786-o stable cell lines treated with 5 μ g/mL of ISD90 for indicated periods. Error bars represent SD, n = 3. (C) IB analyses of 293T cells transfected with indicated constructs and treated with 3 μ M of diABZI for 4 hrs. (D) IB analyses of control and CK1 γ 1

depleted 786-o cells treated with 5 μ g/mL of ISD90 for indicated periods. (E) IB analyses of 293T cells transfected with indicated constructs. (F) IB analyses of STING-reconstituted 786-o cells treated first with 40 μ M of D4476 for 24 hrs and then with 3 μ M of diABZI for indicated periods. (G) RT-PCR analyses of IFNB1 mRNA in 786-o cells treated first with 40 μ M of D4476 for 24 hrs and then with 3 μ M of diABZI for indicated periods. (H) Schematic of STING stabilization resulting from SPOP depletion, CK1 γ 1 inhibition and STING-T356M and increased sensitivity to DNA and STING agonist for type-I interferon signaling activation. One-way ANOVA followed by Tukey's multiple comparison test (B), two-tailed unpaired Student's t test (G). *p < 0.05. Representative experiments shown in figures were repeated at least two times independently with similar results.

Figure 7. Pharmacological SPOP inhibition induces DNA damage to trigger STING activation. (A) IB analyses of WCL and GST pulldown products derived from 293T transfected with indicated constructs and treated with indicated dose of 6lc and 10 μ M of MG132 for 12 hrs. (B and C) IB analyses of B16 and A2058 cells treated with indicated dose of 6b for 24 hrs. (D and E) RNA expression profiling heatmap of genes in type-I interferon response in A2058 cells (D) and B16 cells (E) treated with 10 μ M of 6lc for 24 hrs. (F and G) B16 cells were treated with indicated dose of 6lc for 24 hrs and examined using alkaline lysis method to detect single-strand breaks. Microscopic images of representative comets (F) and tail moment quantification (G) are shown. Error bars represent SD, 0 μ M, n = 54; 5 μ M, n = 50; 10 μ M, n = 56. *p < 0.05 compared with 0 μ M (unpaired t test). (H-K) B16 cells and A2058 cells were treated with indicated dose of 6b or 6lc for 24 hrs before immunofluorescence of γ H2AX (H and J) and quantification of percentages of γ H2AX positive cells (I and K). Error bars represent SD, n = 5-7. *p < 0.05

compared with 0 μ M (unpaired t test). One-way ANOVA followed by Dunnett's multiple comparison test (G), Fisher's LSD test (K), two-tailed unpaired Student's t test (I). *p < 0.05. Representative experiments shown in figures were repeated at least two times independently with similar results.

Figure 8. Genetic SPOP depletion mildly induces DNA damage. (A) Immunofluorescence of dsDNA in A2058 cells treated with indicated dose of 6b or 6lc for 24 hrs. (B) RT-PCR analyses of mRNA changes in B16 cells treated with indicated dose of 6b for 24h hrs. Error bars represent SD, n = 3. (C) RT-PCR analyses of mRNA changes in control and STING knockout B16 cells treated with indicated dose of 6lc for 24h hrs. Error bars represent SEM, n = 2. (D and E) Immunofluorescence of γ H2AX in control and SPOP depleted A2058 cells and quantification of percentages of γ H2AX positive cells. Error bars represent SD, n = 4-8. Unpaired t test determined no statistical significance between any groups. (F) Schematic illustration of the impact of SPOP depletion and 6b/6lc treatment on the function of SPOP protein. One-way ANOVA followed by Fisher's LSD test (E) or Tukey's multiple comparison test (B and C). *p < 0.05. Representative experiments shown in figures were repeated at least two times independently with similar results.

Figure 9. Systematic profiling of the protein degradation landscape induced by SPOP inhibition. (A) Schematic diagram of the hypothesis that 6lc binding to SPOP not only disrupts SPOP interactions with its bona fide substrates, resulting in STING accumulation, but also recruits neo-substrates to SPOP for regulation, which triggers DNA damage, STING activation and immune response. (B) Workflow of detecting 6lc-induced protein ubiquitination. Control and SPOP depleted A2058 cells were lysed after 12 hrs treatment of 10 μM of 6lc. Ubiquitinated

peptides with di-glycine tag resulting from trypsin digestion were enriched by K-ε-GG immunoaffinity beads, followed by quantitative LC-MS/MS analysis. Candidates regulating DNA damage was selected from 6lc-induced SPOP-dependent ubiquitinated proteins for validation. (C) Selection of candidates from all ubiquitinated proteins significantly changed upon 6lc treatment. Left volcano plot shows K-ε-GG peptides significantly changed (q-value <0.05, log2 fold change < -0.6 or > 0.6) in shScr cells after 6lc treatment. Hits in blue were peptides of SPOP substrates downregulated after 6lc treatment. Middle Venn diagram shows among 11502 peptides belonging to 3625 proteins, 221 peptides belonging to 182 proteins were at least two folds more enriched (1) in shScr+6lc than in shScr, (2) in shScr+6lc (vs shScr) than in shSPOP+6lc (vs shScr) and (3) in shScr+6lc (vs shScr) than in shSPOP+6lc (vs shScr) than in shSPOP+6lc (vs shScr) and WCL derived from HA-Ub-expressing A2058 cells treated with 10 μM of 6lc and 10 μM of MG132 for 12 hrs. Arrowheads indicate positions of full-length proteins. Representative experiments shown in figures were repeated at least two times independently with similar results.

Figure 10. CBX4 is a neo-substrate for SPOP/6lc to control DNA damage. (A) IB analyses of A2058 cells treated with 20 μM of 6lc for indicated periods. On the right side are starting time points of protein level changes. (B) IB analyses of control and SPOP depleted A2058 cells treated with 20 μM of 6lc for indicated periods. (C) IB analyses of control and CUL3 depleted 786-o cells treated with 20 μM of 6lc for 12 hrs. (D) IB analyses of control and SPOP depleted A2058 cells. (E) RT-PCR analyses of A2058 cells treated with 20 μM of 6lc for indicated periods. Error bars represent SD, n=3. No statistical significance between any groups (two-tailed unpaired Student's t test). (F) In vitro Streptavidin pulldown assay using indicated dose of compounds and purified

proteins. (G) Schematic of CBX4 backbone, SUMO-interacting motifs SIM1 and SIM2, and truncations used in (H). Full-length CBX4 consists of chromodomain (CD), two intrinsically disordered domains P2 and P3 and CBox domain. (H) IB analyses of HA-CBX4-FL and truncations in A2058 cells upon 20 µM of 6lc treatment for indicated periods. Quantification of relative HA grayscales is shown. Representative experiments shown in figures were repeated at least two times independently with similar results.

Figure 11. 6lc triggers DNA damage through the CBX4/BMI1/H2A axis. (A) IB analyses of control and CBX4 depleted A2058 cells. (B) IB analyses in control and CBX4-overexpressing A2058 cells treated with 20 μM of 6lc for 12 hrs. (C to I) γH2AX immunofluorescence (C), dsDNA immunofluorescence (E), RT-PCR analyses (G), and BMI1/CBX4 immunofluorescence (H) in control and CBX4-overexpressing A2058 cells treated with 20 μM of 6lc for 12 hrs. Error bars represent SD, n=8 (D), n=14-21 (F), n=3 (G), n=55-65 (I and J). (K) IB analyses of BMI1-IP and WCL derived from A2058 cells overexpressing CBX4-WT and -ΔSIM1/2. (L) A schematic diagram of 6lc-mediated CBX4 degradation, DNA damage and STING activation. Detailed information is given in the Results section. One-way ANOVA followed by Tukey's multiple comparison test (D, F and G), Kruskal-Wallis test followed by Dunn's test (I and J). *p < 0.05. Representative experiments shown in figures were repeated at least two times independently with similar results.

Figure 12. SPOP inhibition enhances immunotherapy effects in murine models. (A) Schematic of the syngeneic B16 melanoma model in which tumor-bearing mice are treated with/without 6b for analysis single RNA sequence. (B) Uniform Manifold Approximation and

Projection (UMAP) plot of cells profiled from both two groups; clusters are annotated based on expression patterns of characteristic genes. (C) Composition of each cluster from (A). (D) Tumor volume measurements at indicated days after cell inoculation. Arrowheads indicate treatment schedule of indicated agents. Error bars represent SEM. Vehicle, 6b and Anti-PD-1: n = 9; Combo: n = 8. (E) Representative images of tumors isolated from (D). (F to J) The absolute percentages of T cells (F), CD4+ T cells (G), MFI of IFN γ in CD4+ cells (H), CD8+ T cells (I), and percentage of Gramzym B (GrzB)+ cells in CD8+ T cells (J) in implanted B16 tumors from mice treated with indicated agents was analyzed by flow cytometry. Error bars represent SEM, n = 8 (H); Vehicle, 6b and Anti-PD-1: n = 7; Combo: n = 6 (F, G, I and J). Two-way (D) or one-way ANOVA (F-J) followed by Tukey's multiple comparison test. *p < 0.05, **p < 0.01.

Figure 13. The enhanced immunotherapeutic effects of SPOP inhibition depend on tumor-intrinsic STING. (A) Tumor volume measurements at indicated days after cell inoculation. Arrowheads indicate treatment schedule of indicated agents. Error bars represent SEM. n = 7. (B) Representative images of tumors isolated from (A) and weighed in (C). (D) Kaplan-Meier survival curve of anti-PD-1 treated melanoma patients with high or low expression of SPOP mRNA. The image is based on the SPOP-Melanoma-PRJEB23709_anti-PD-1-None-None-0.5-survival dataset in TIGER (Tumor Immunotherapy Gene Expression Resource) database. Two-way ANOVA followed by Tukey's multiple comparison test (A), One-way ANOVA followed by Fisher's LSD test (C).

Figure 14. SPOP inhibition enhances CAR-T cell effects in xenografted B16 melanoma models. (A) Schematic of the B16-OVA-hCD19 melanoma model in which tumor-bearing mice

were lymphodepleted with cyclophosphamide (Cy) and then treated with CAR.CD19 T cells intravenously (i.v.). And following with/without 6lc treatment 5 times, every 2-3 days. (B) Measurement of the tumor volume at indicated days after cell inoculation. Arrowheads indicate treatment schedule of indicated cells and agents. Error bars represent SEM. CAR.CD19-T: n=4; CAR.CD19-T+6lc, n=5. (two-way ANOVA followed by Tukey's multiple comparison test). (C) Representative images of tumors isolated from (B). (D to H) Percentages of CAR-T (D), CD4 (E), CD8 (F), NK (G), macrophages (H) in CD45+ cells from B16-OVA-hCD19 tumors in (B). Error bars represent SEM. Vehicle: n=4; 6lc: n=5. **p < 0.01 (two-tailed unpaired Student's t test).

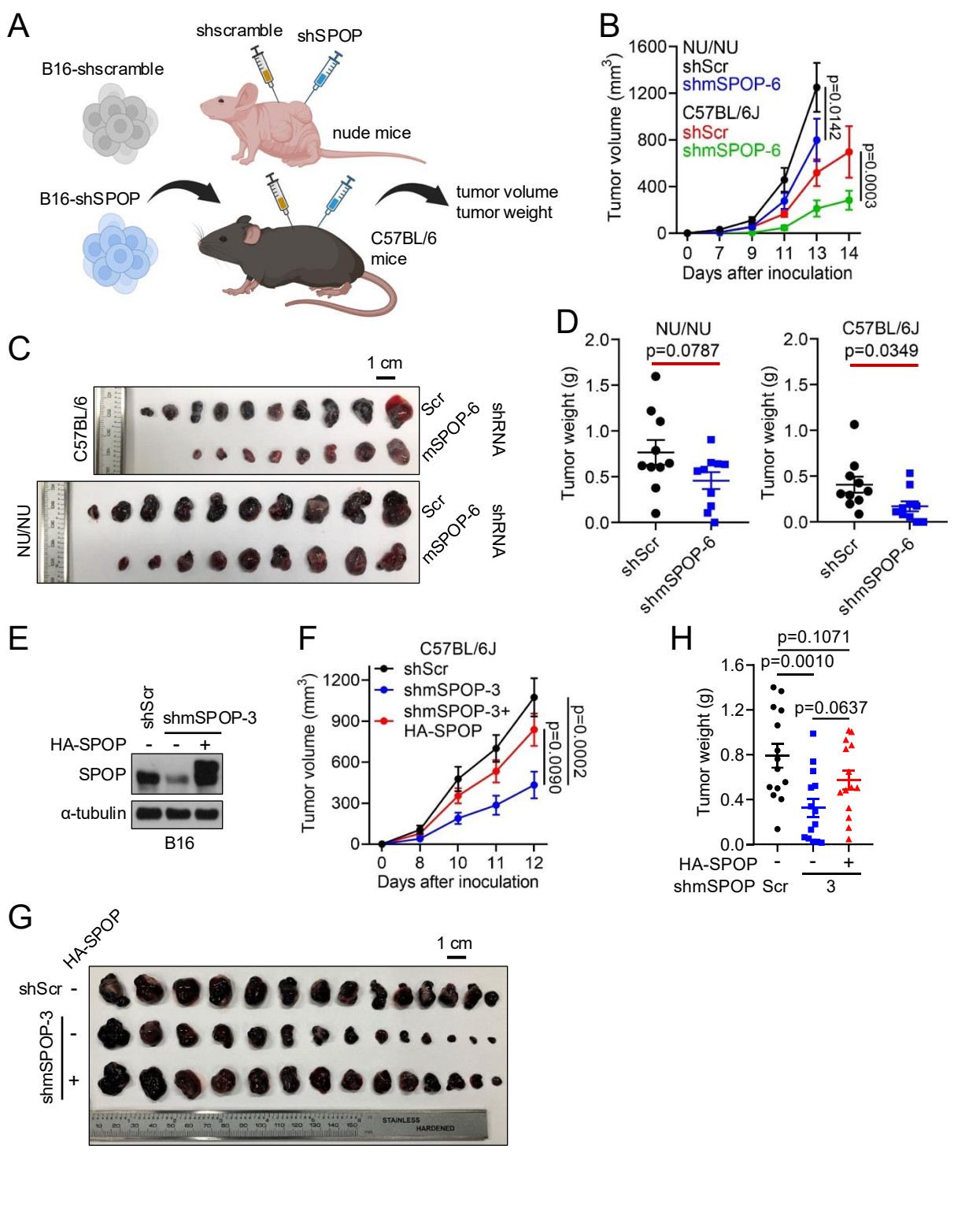


Figure 1

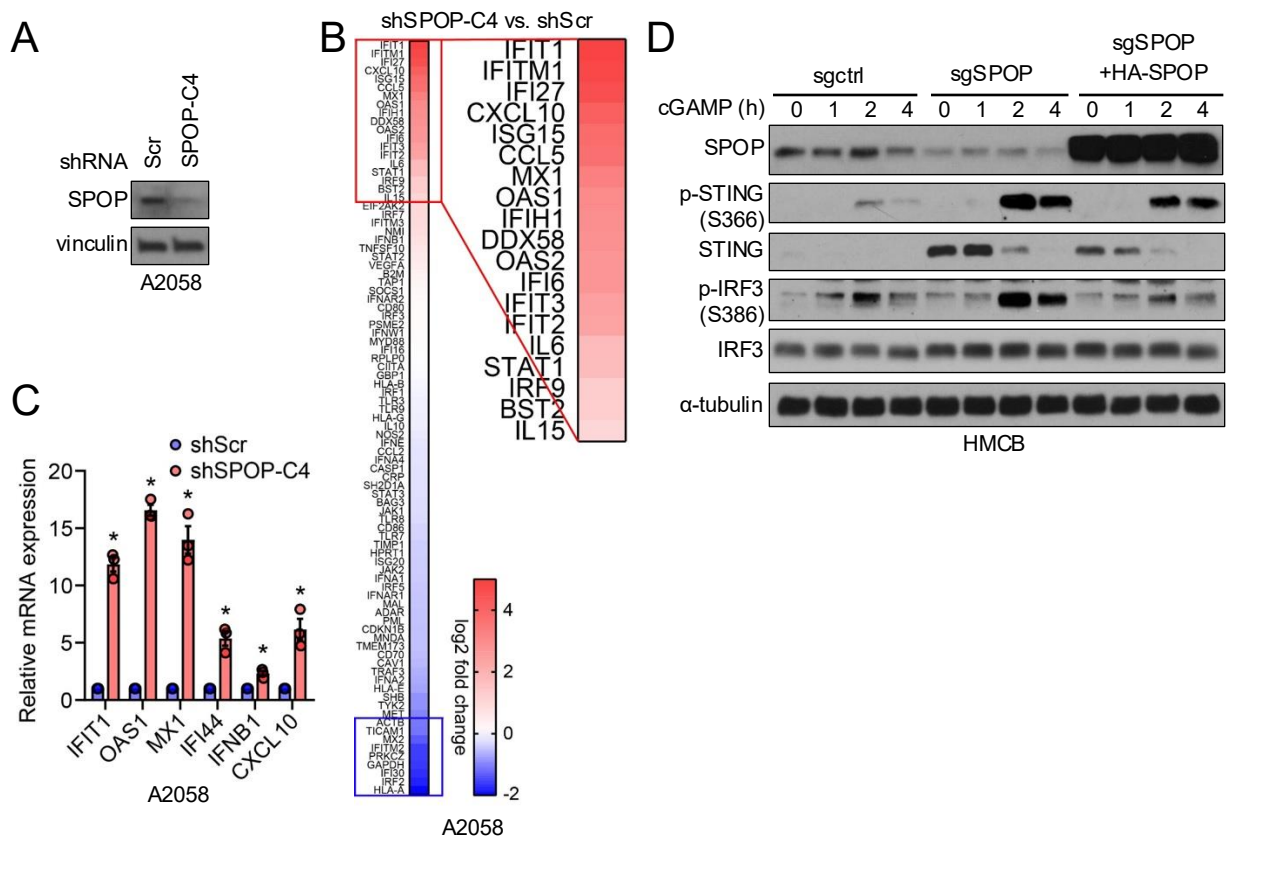


Figure 2

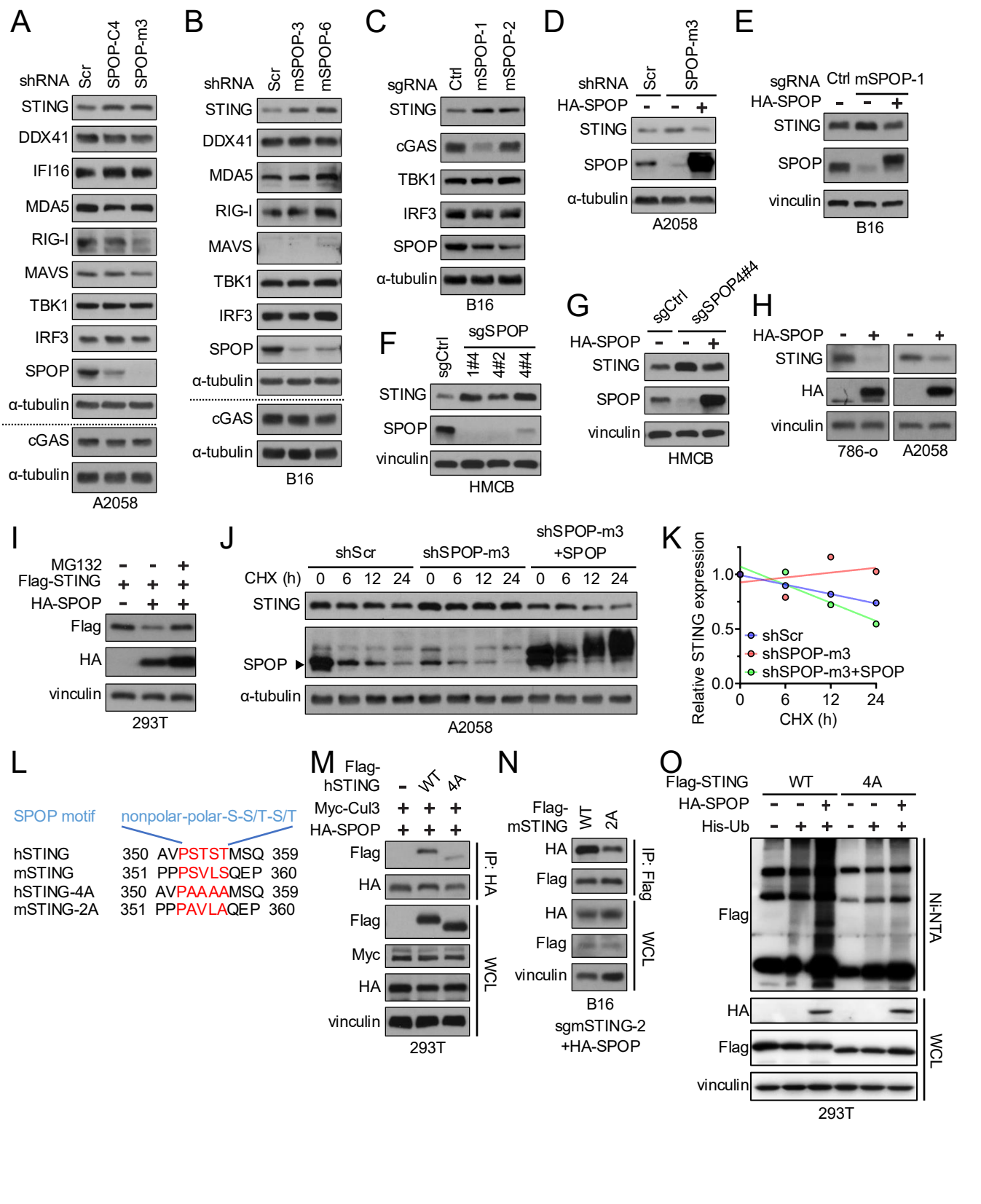


Figure 3

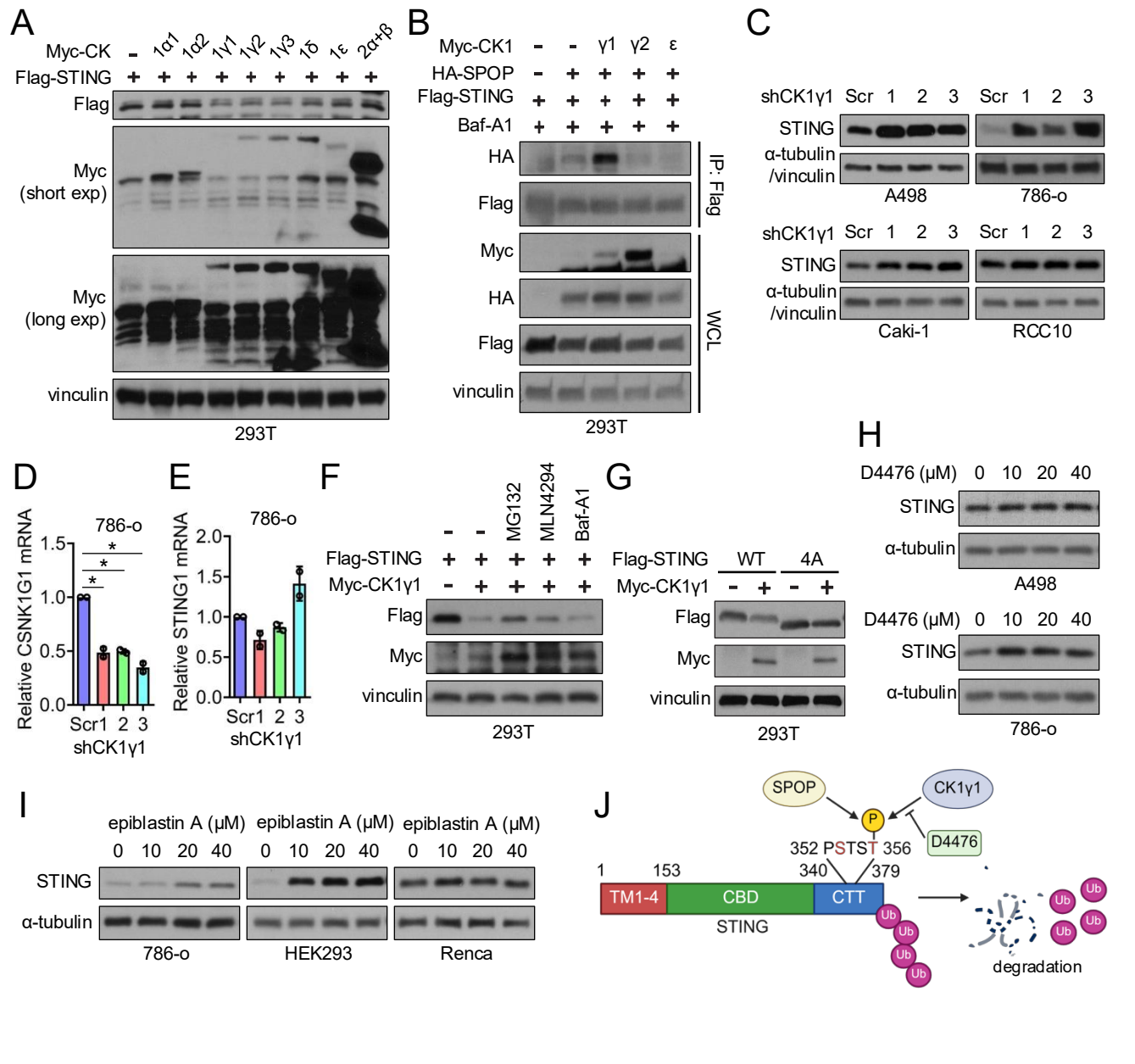


Figure 4

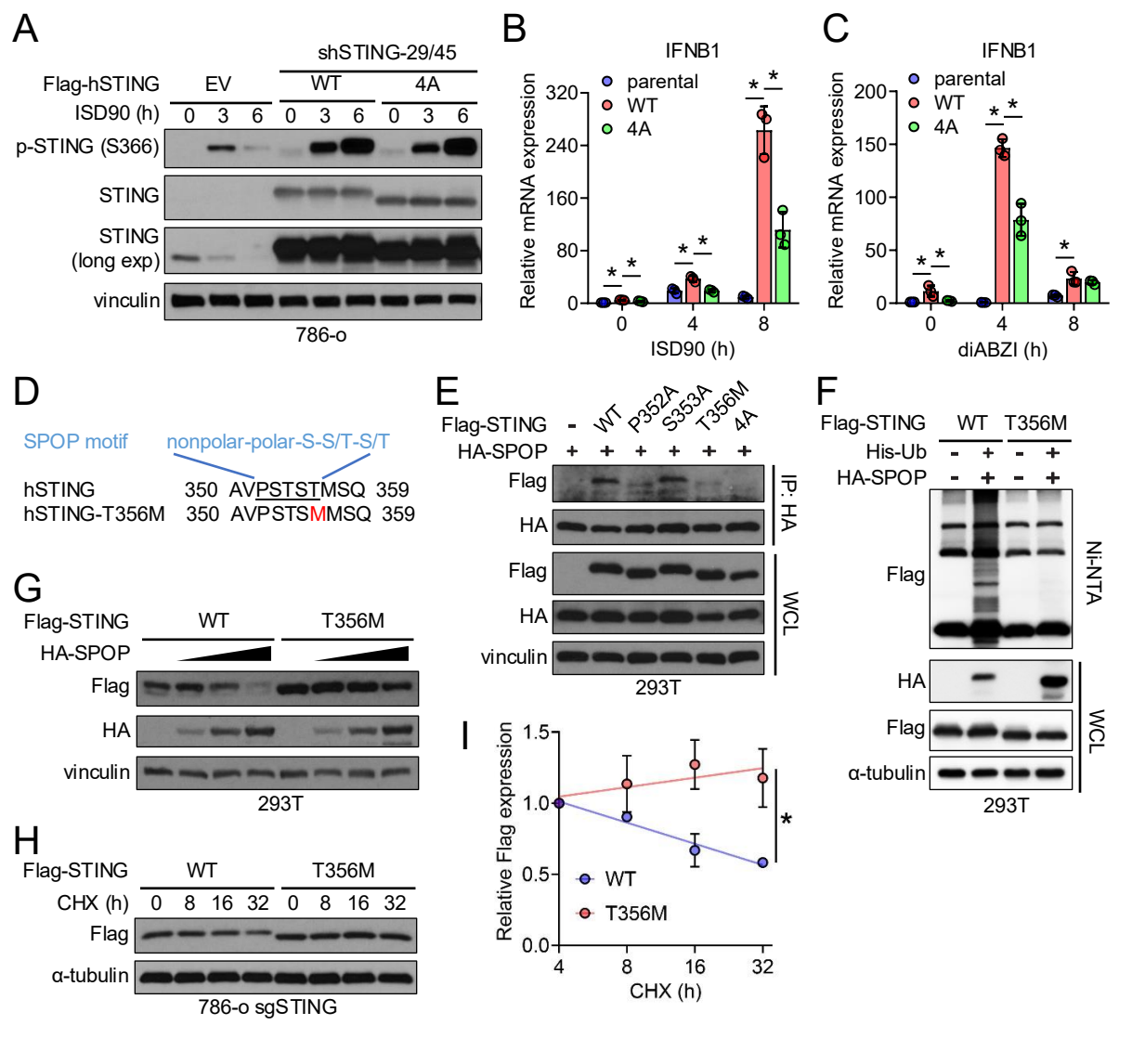


Figure 5

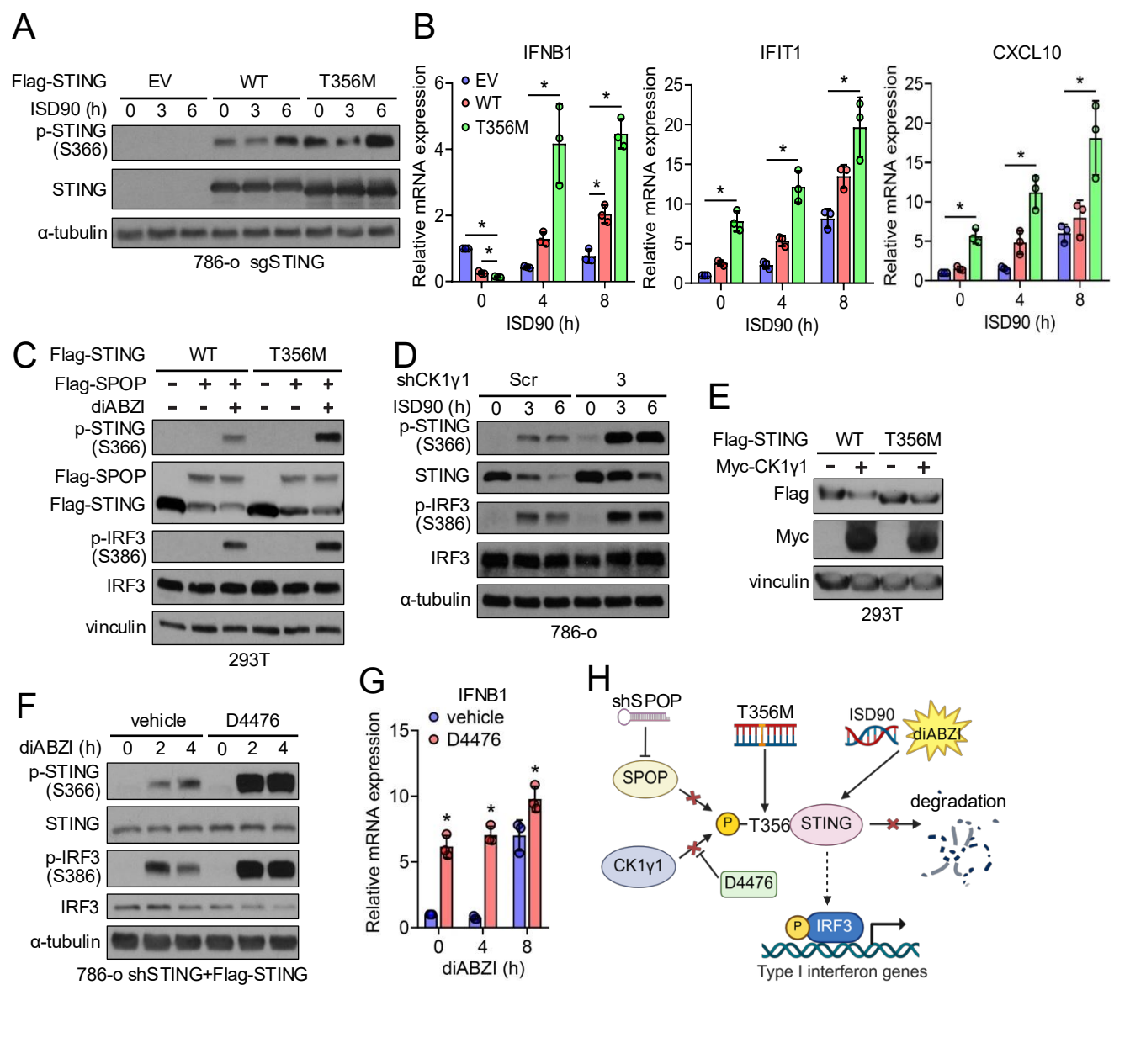
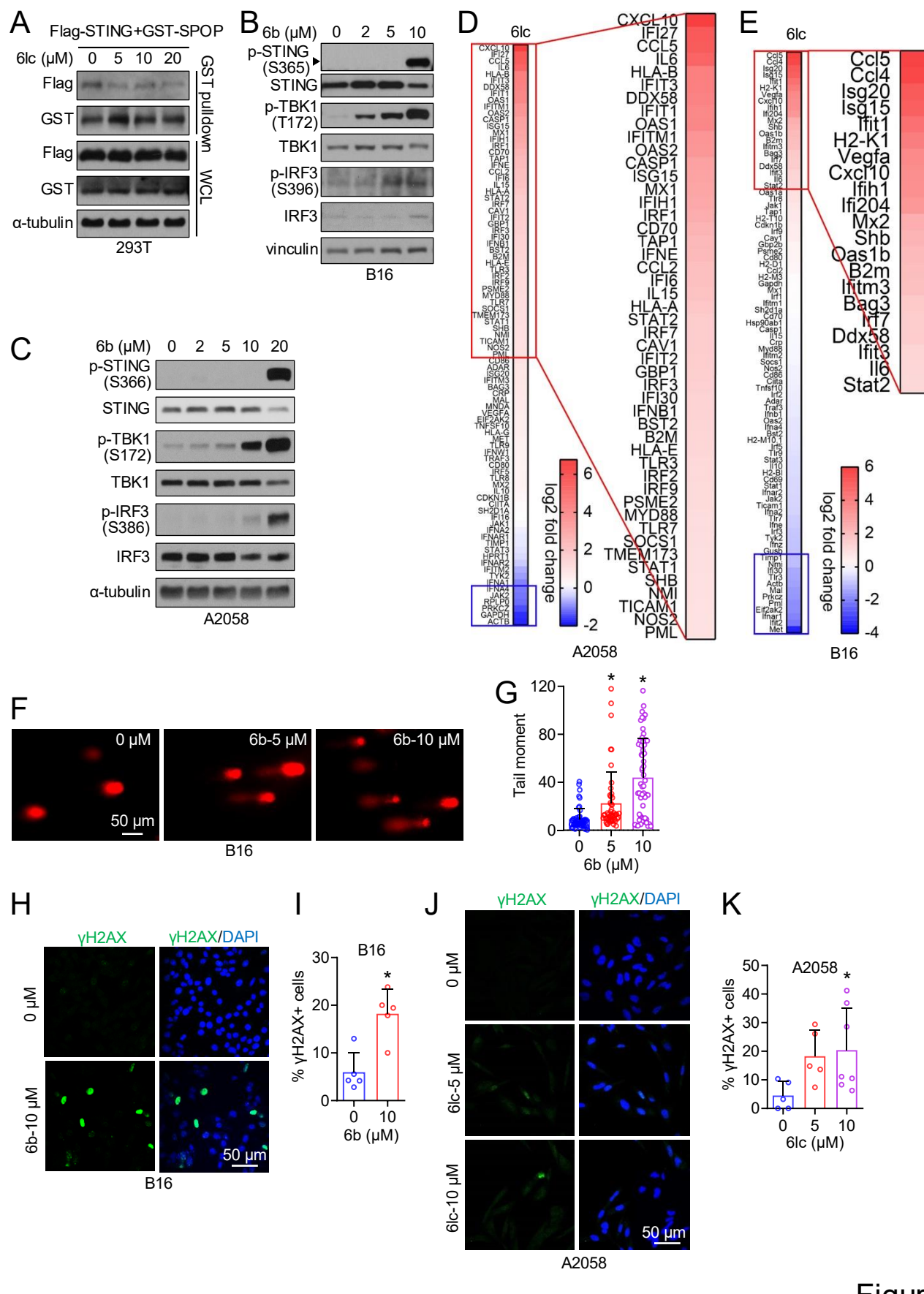


Figure 6



D

6lc

Ε

6lc

Figure 7

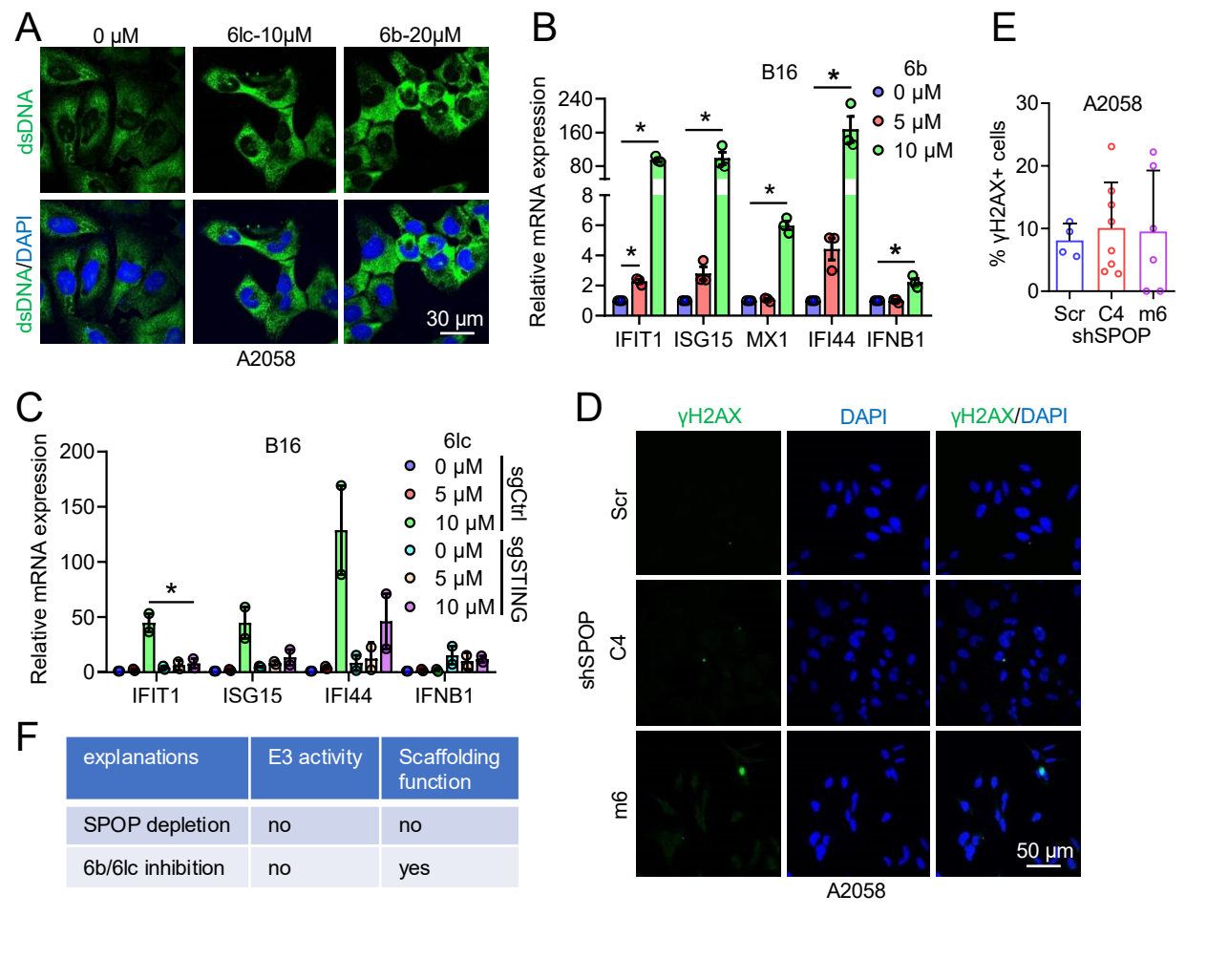


Figure 8

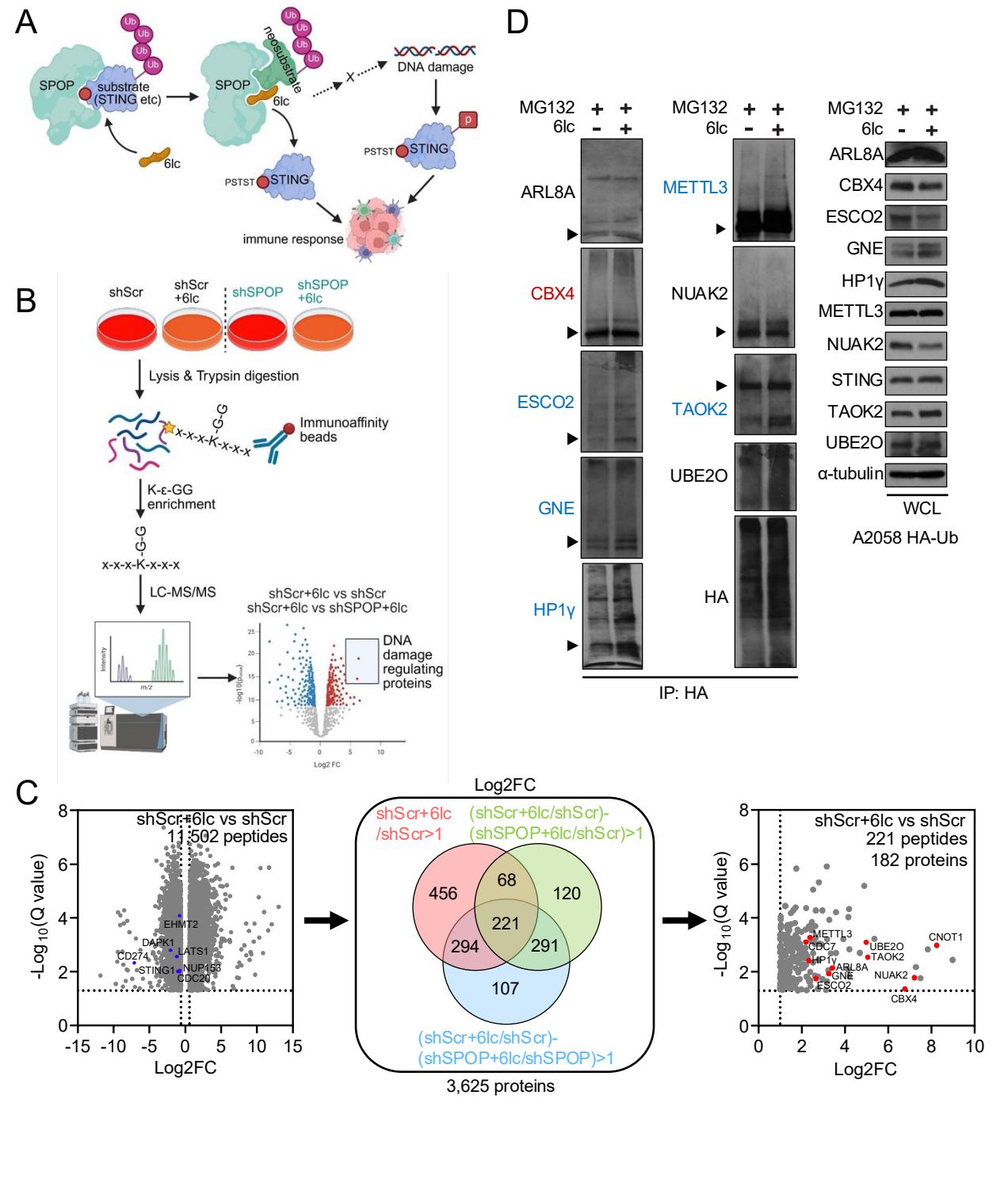


Figure 9

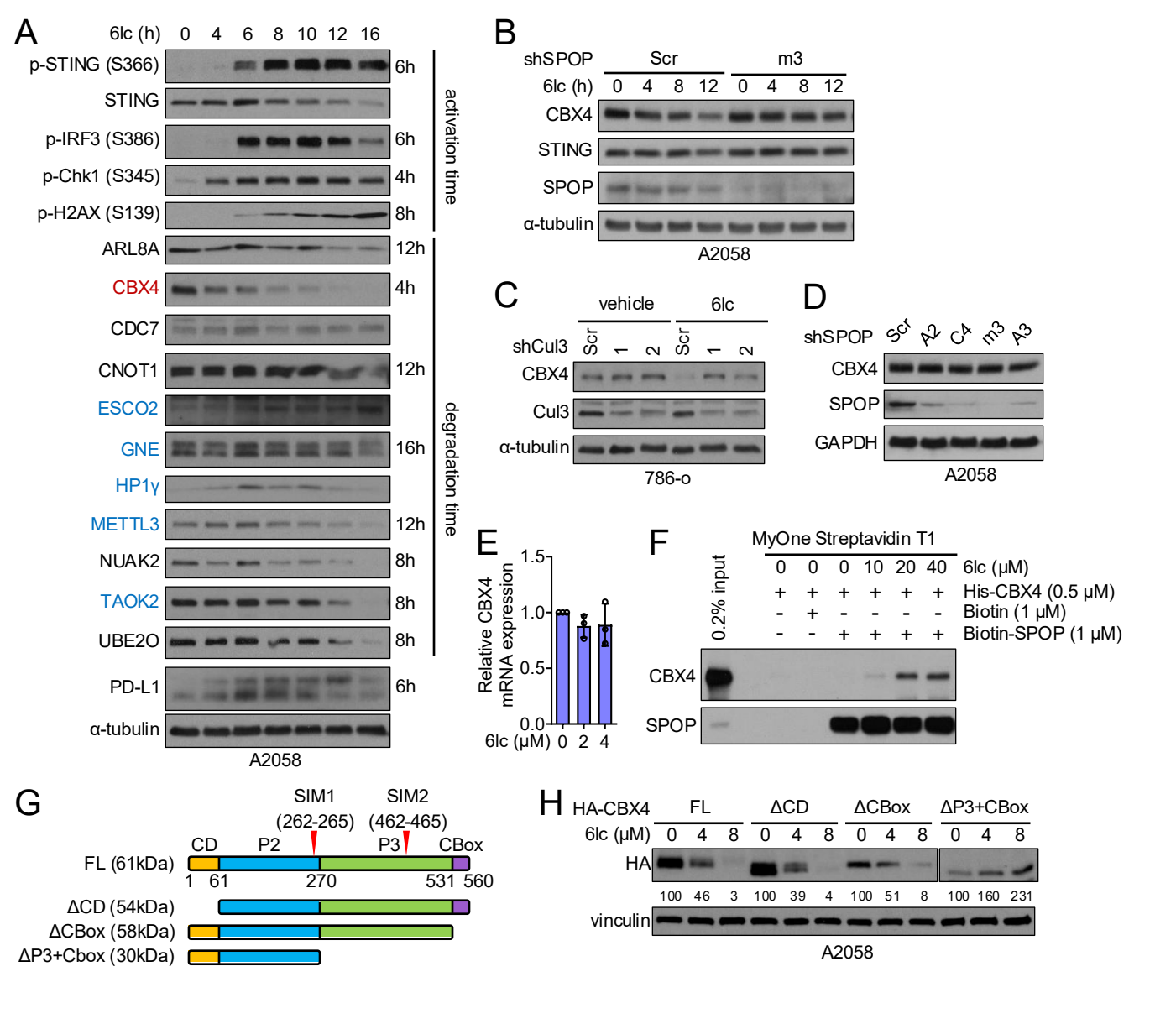


Figure 10

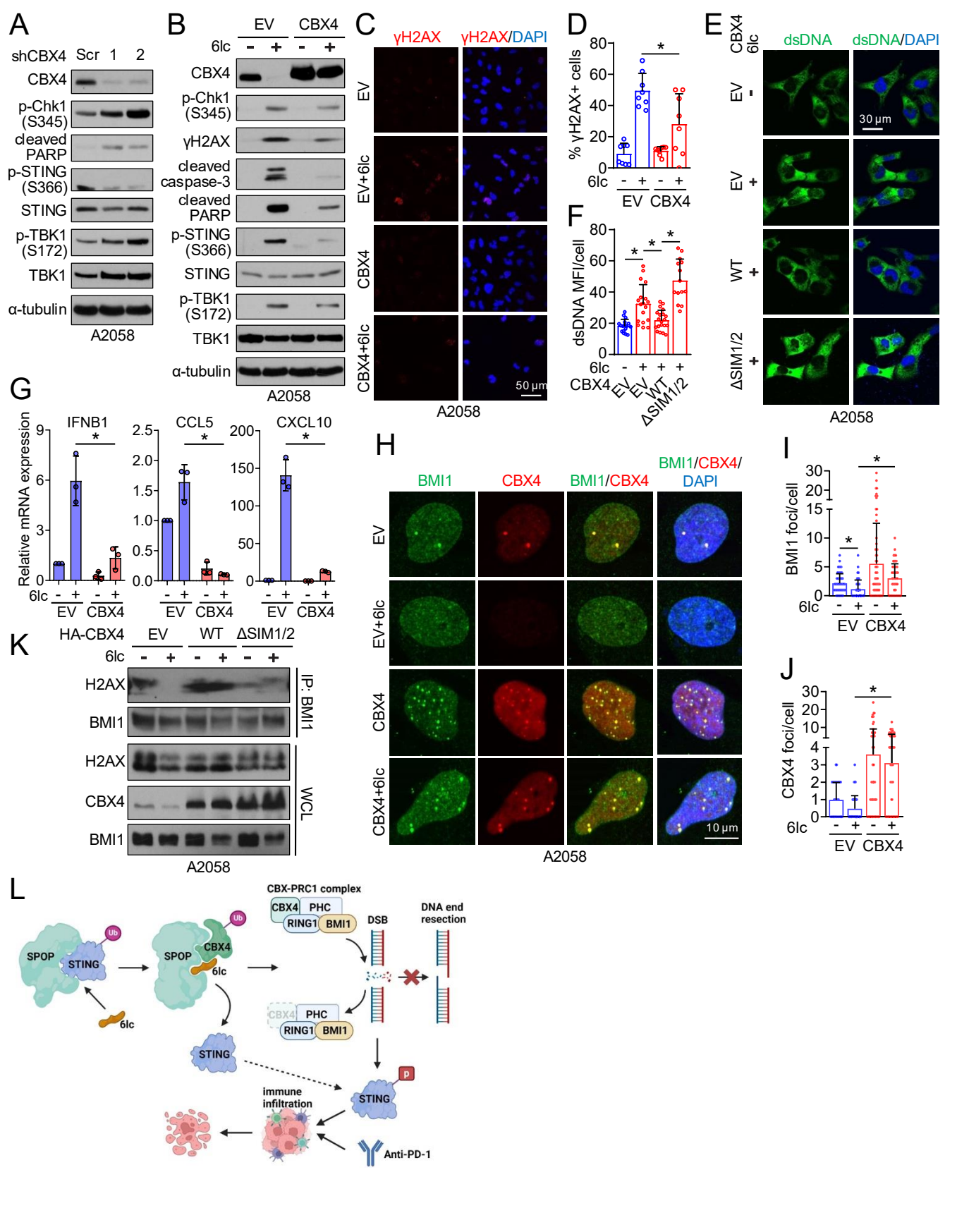


Figure 11

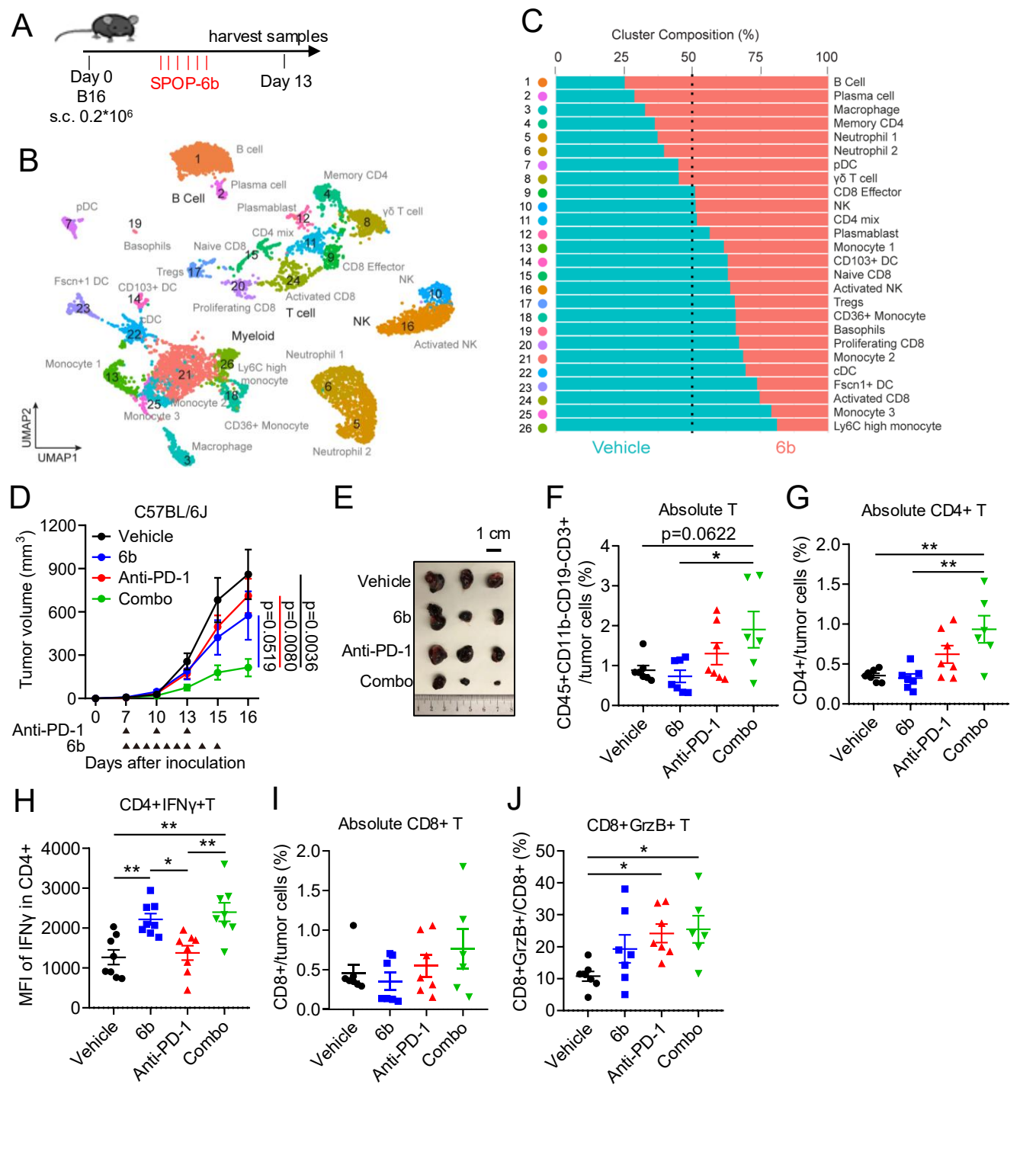


Figure 12

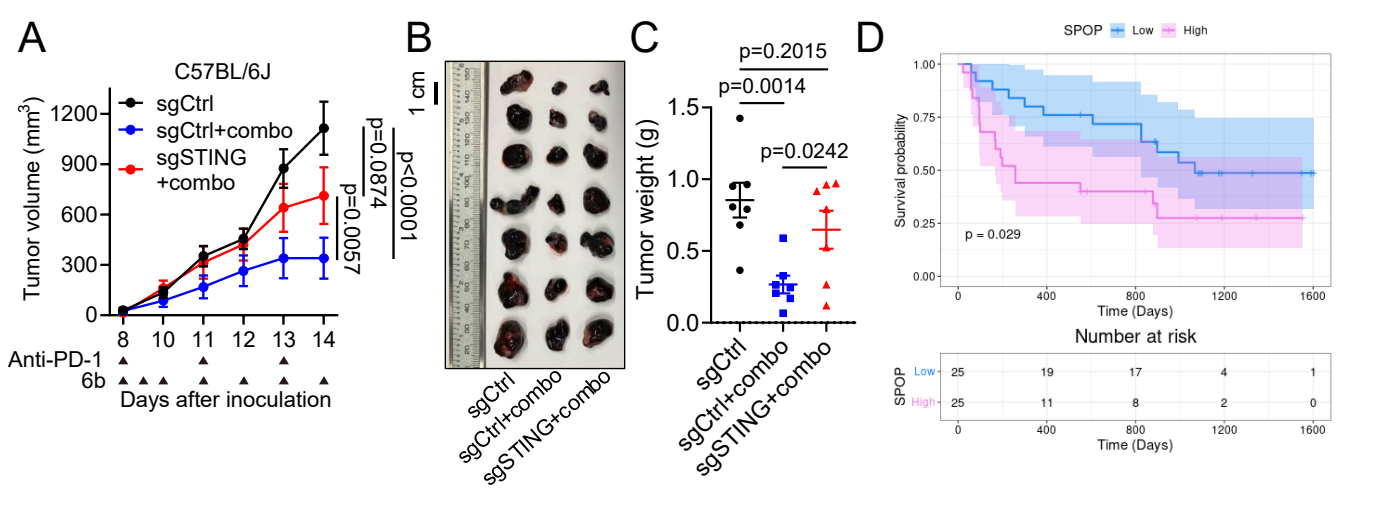


Figure 13

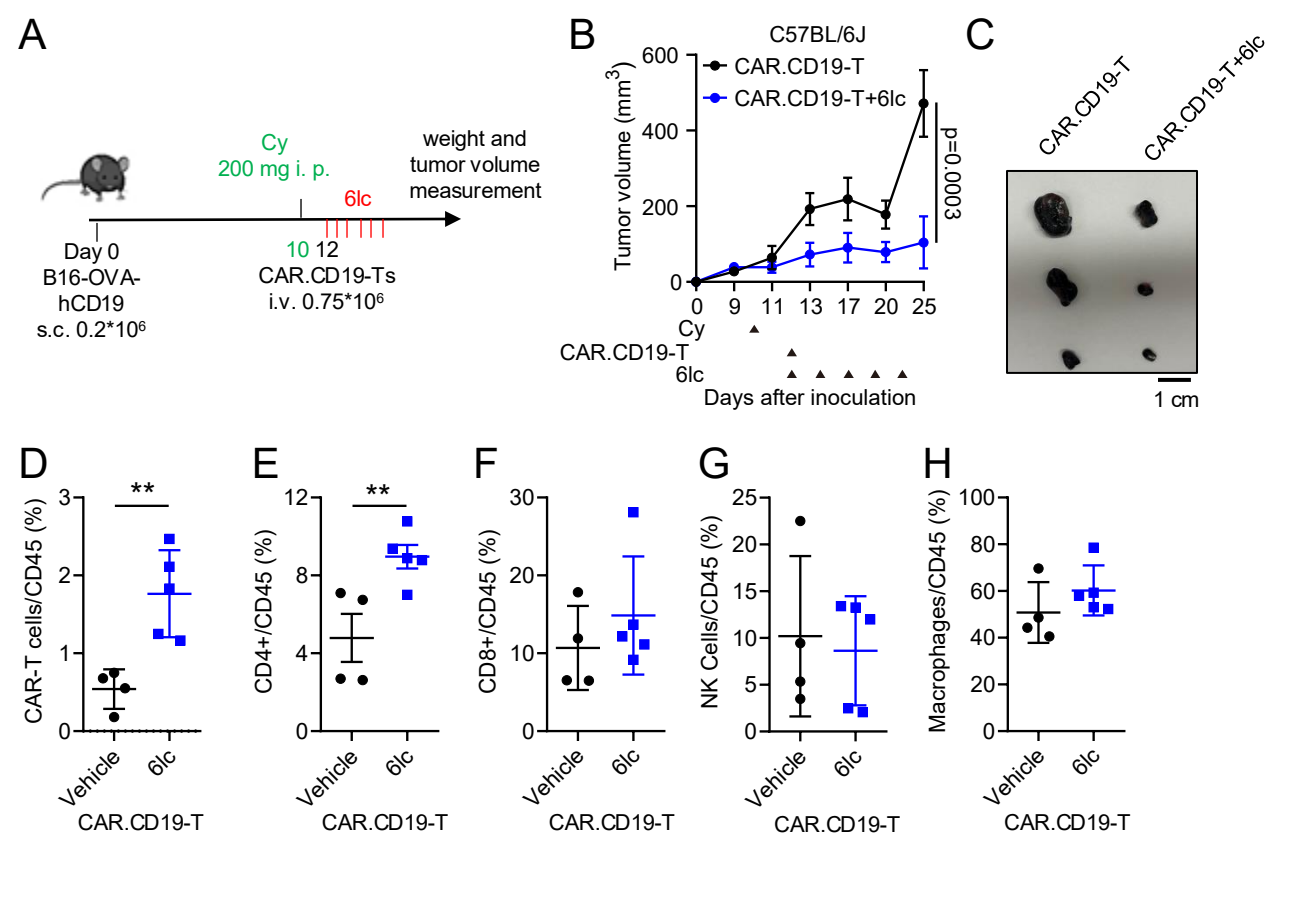


Figure 14